Schweizerischer Erdbebendienst
Service Sismologique Suisse
Servizio Sismico Svizzero
Swiss Seismological Service

ETH zürich

SITE CHARACTERIZATION REPORT

STHK: Thun (BE) - Gymnasium Schadau

Manuel Hobiger, Paolo Bergamo, Clotaire Michel, Donat Fäh

Last Modification: 3rd March, 2020

Schweizerischer Erdbebendienst (SED)
Service Sismologique Suisse
Servizio Sismico Svizzero
Servizi da Terratrembels Svizzer

ETH Zürich
Sonneggstrasse 5
8092 Zürich
Schweiz
manuel.hobiger@sed.ethz.ch

Contents

1 Summary

The free-field strong-motion station STHK was built next to the Kantonsschule in Thun (BE). We performed two passive seismic array measurements with different size for the site characterization. These measurements show that the fundamental frequency of the structure beneath the station is about 0.75 Hz.
The array measurements were analyzed with three different techniques, namely 3-component high-resolution FK (HRFK), WaveDec and SPAC. All techniques gave similar dispersion curves. The dispersion curves for the fundamental and first harmonic modes of both Love and Rayleigh waves could be retrieved, where the measurements in the larger array reproduced the fundamental modes and the smaller arrays the first harmonic modes. Joint inversions of dispersion and ellipticity curves yielded a surficial layer of around 7 m thickness with a shear-wave velocity of about 200 m/s, followed by a second layer of around 500 m/s down to about 150 to 200 m, where the seismic bedrock is found. The V_{S30} value is around 370 m/s (ground type B in EC8 and C in SIA261).

2 Introduction

In the framework of the second phase of the Swiss Strong Motion Network (SSMNet) renewal project, a new station was planned in the city of Thun (BE). The site selection resulted in the Gymnasium Schadau as the best site from the risk and noise aspects. The new station, called STHK, was constructed between the school building and the KKThun (Kultur- und Kongresszentrum) and went operational on 21 April 2015. The location of the station is shown in Fig. 1.

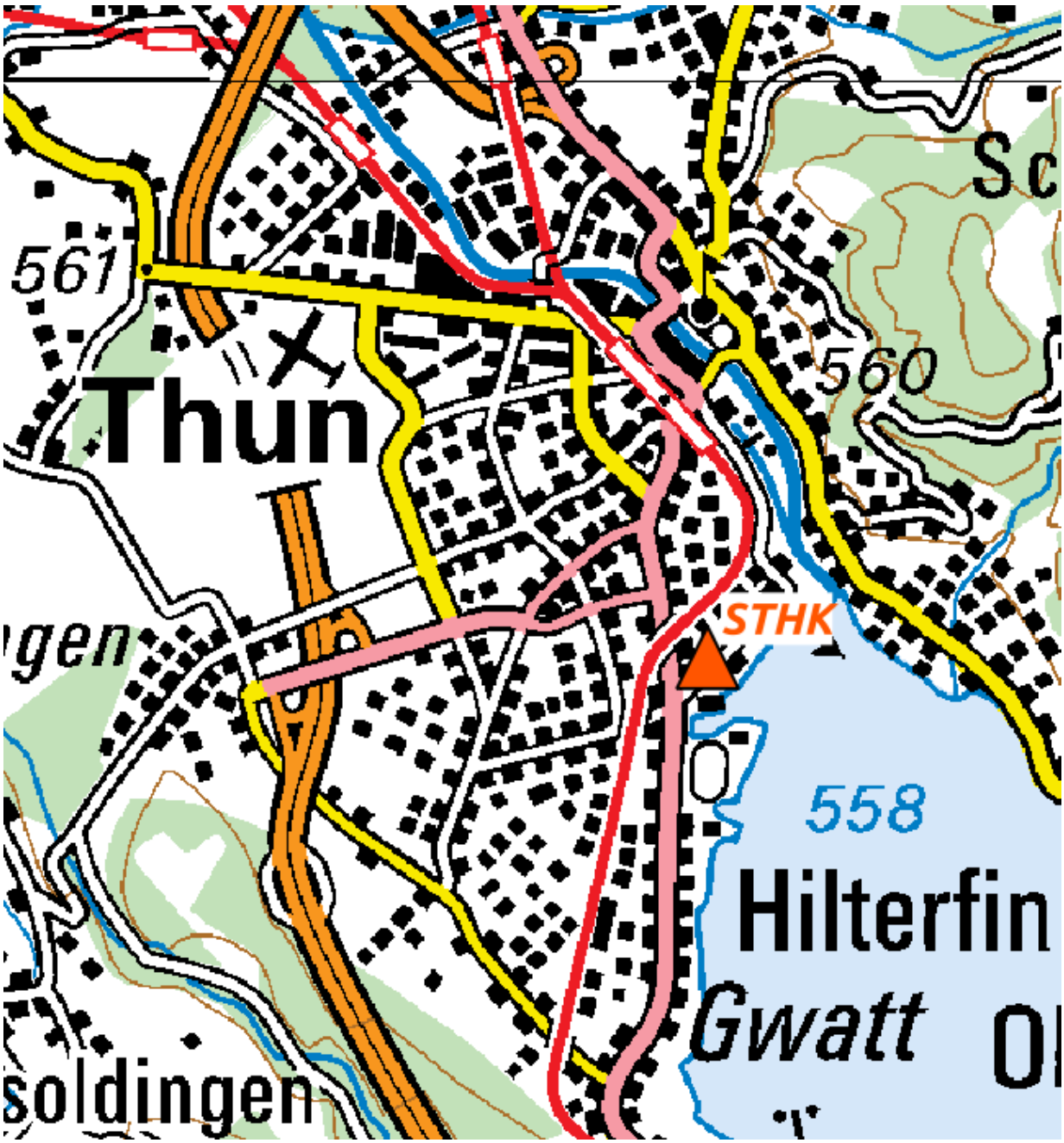

Figure 1: Map showing the location of station STHK in Thun.

3 Geological setting

A geological map of the surroundings of station STHK is shown in Fig. 2. The station is located in the deep basin of the city of Thun.

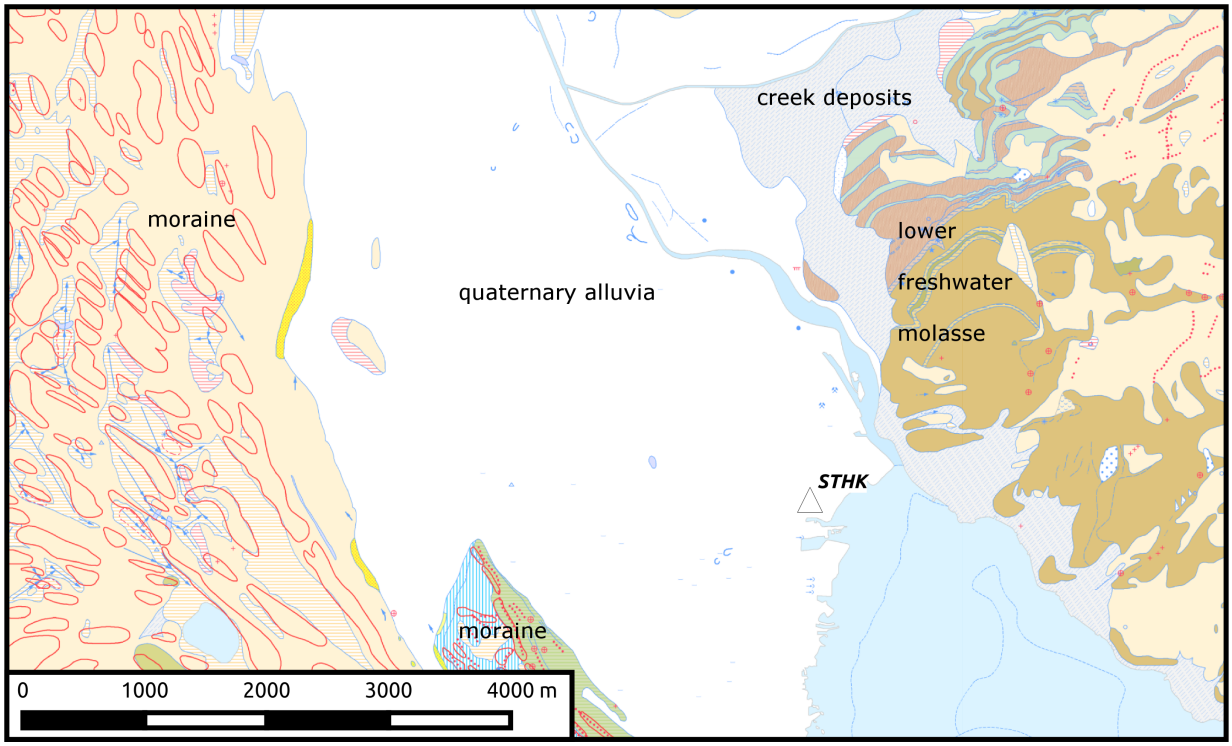

Figure 2: Geological map of the area around station STHK. The main geological formations are labeled in the map.

4 Site characterization

4.1 Measurements and data set

In order to characterize the local underground structure below station STHK, passive seismic array measurements were carried out on 9 July 2015. The layout of the two seismic arrays is shown in Fig. 3.
Due to logistical constrains, the larger array was installed first. This array, named array 1, consisted of 12 stations in total. It was planned as consisting of a central station and two rings of five stations each with radii of 70 and 150 m, respectively. A twelth station was installed close to the seismic station STHK, at the center of the second array. The station names of this first array are composed of "STHK" followed by a two-digit number between 01 and 29.
The smaller array, labelled array 2, was built with 14 stations. The layout of the second array was less regular. It had an inner ring of 12 m diameter composed of five stations around a central station. A second ring with a radius of 28 m was composed of three stations. The other stations of the second array were distributed further away and less systematically due to the limited available space. The station names of the second array consist of "STHK" followed by a two-digit number between 51 and 81.
The parameters of both arrays are given in Table 1.
The station locations were measured by a differential GPS system (Leica Viva GS10) which was set up to measure with an uncertainty lower than 5 cm. All station locations except three were measured with better precisions than this. Station STHK29 of array 1 had a precision of 0.62 m. In the second array, station STHK79 was measured with a precison of 0.13 m and station STHK78 with a precision of 0.12 m.

Table 1: List of the seismic array measurements in Thun.

Array name	Number of sensors	Minimum interstation distance [m]	Maximum interstation distance [m]	Recording time [s]
1	12	28.6	293.9	7200
2	14	11.8	85.3	5340

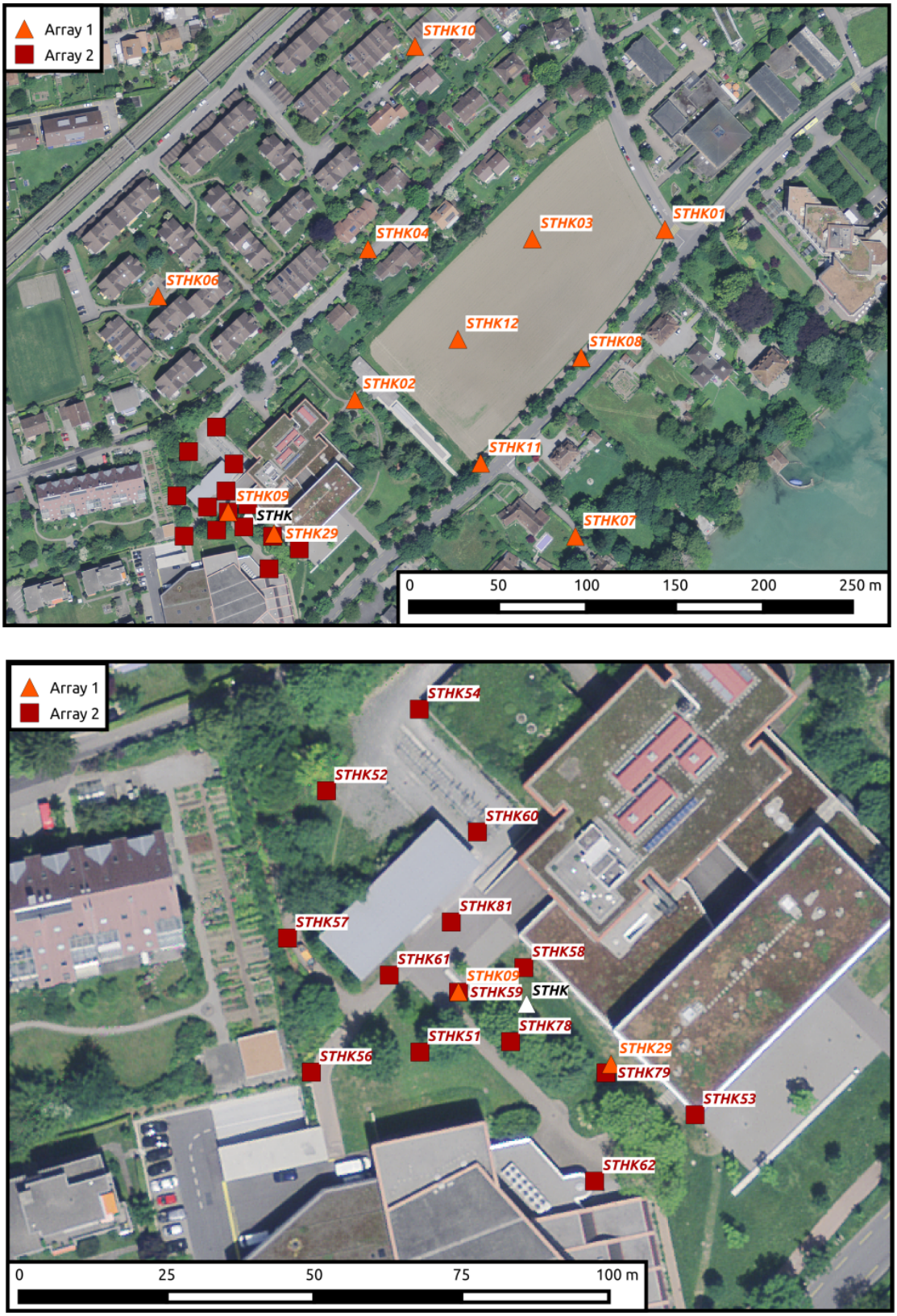

Figure 3: Layout of the array measurements around station STHK. The location of STHK is indicated by the white triangle, the locations of the stations during the first array measurement by orange triangles and during the second array measurement by red squares. ©2017 swisstopo (JD100042)

4.2 Measurement results

4.2.1 H/V curves

Figure 4 shows the H/V curves determined with the time-frequency analysis method (Fäh et al., 2009) for all stations of both arrays. In both arrays, the curves are virtually identical between about 0.5 and 2 Hz, i.e. around the fundamental peak, which is at 0.75 Hz. The two stations STHK08 and STHK11 in array 1 have deviations from this behaviour, probably caused by the traffic on the main street close to which they were located.

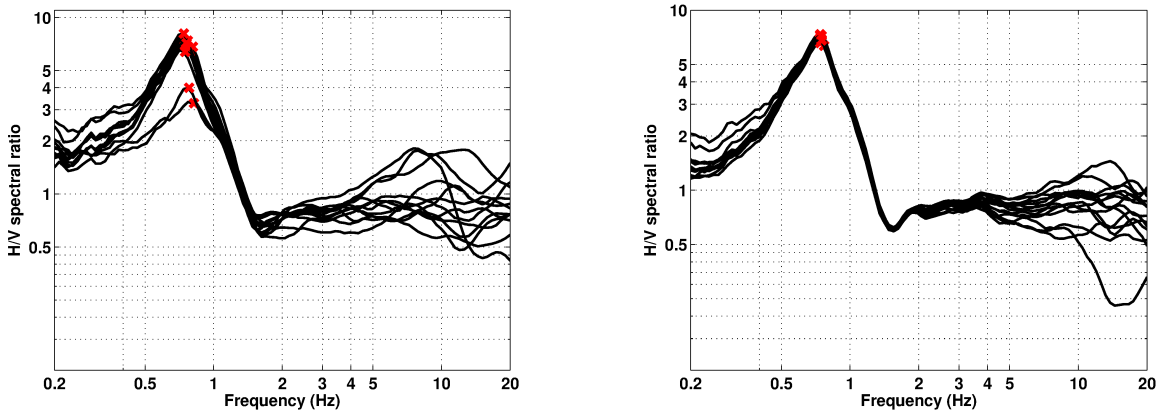

Figure 4: Overview of the H/V measurements for the different stations of the first (left) and the second (right) array measurements.

4.2.2 RayDec ellipticity curves

The RayDec technique (Hobiger et al., 2009) is meant to eliminate the contributions of wave types other than Rayleigh waves and give a better estimate of the ellipticity than the classical H/V technique. The RayDec ellipticity curves for all stations of the array measurements are shown in Fig. 5.
The RayDec curves are similar to the H/V curves and also show very homogeneous results around the peak frequency of 0.75 Hz. In the large array, stations STHK01, STHK08 and STHK11 show differences from the other stations. These three stations are very close to a street with a lot of traffic, which might explain this behavior. The small array seems to have a very homogeneous underground.

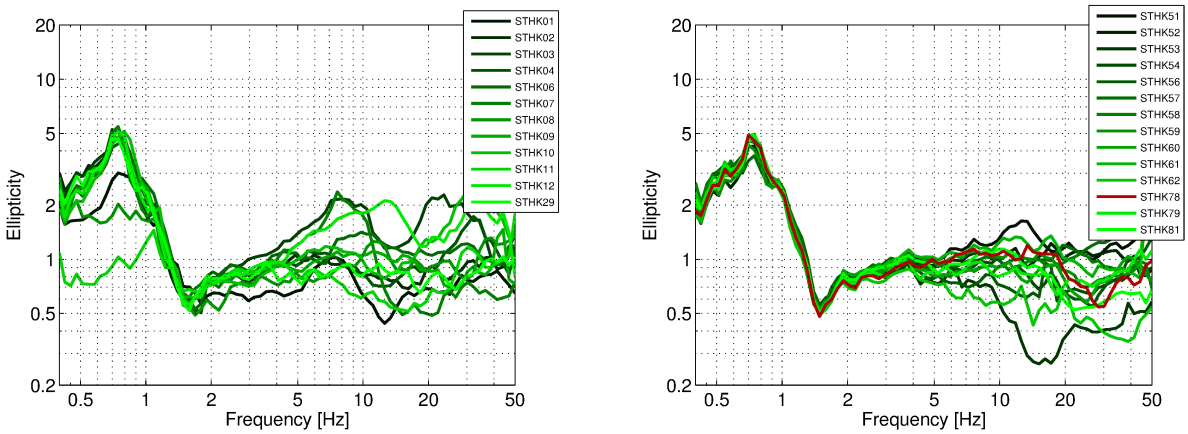

Figure 5: RayDec ellipticities for array 1 (left) and array 2 (right).

4.2.3 Polarization measurements

The polarization parameters of the seismic noise recordings of all stations of the two arrays were estimated according to Burjánek et al. (2010) and Burjánek et al. (2012). Only the results for three stations are shown in Fig. 6.
The particle motion shows linear polarization around the peak frequency of 0.75 Hz, which is expected around the ellipticity peak, but no major 2-dimensional site effects can be seen.

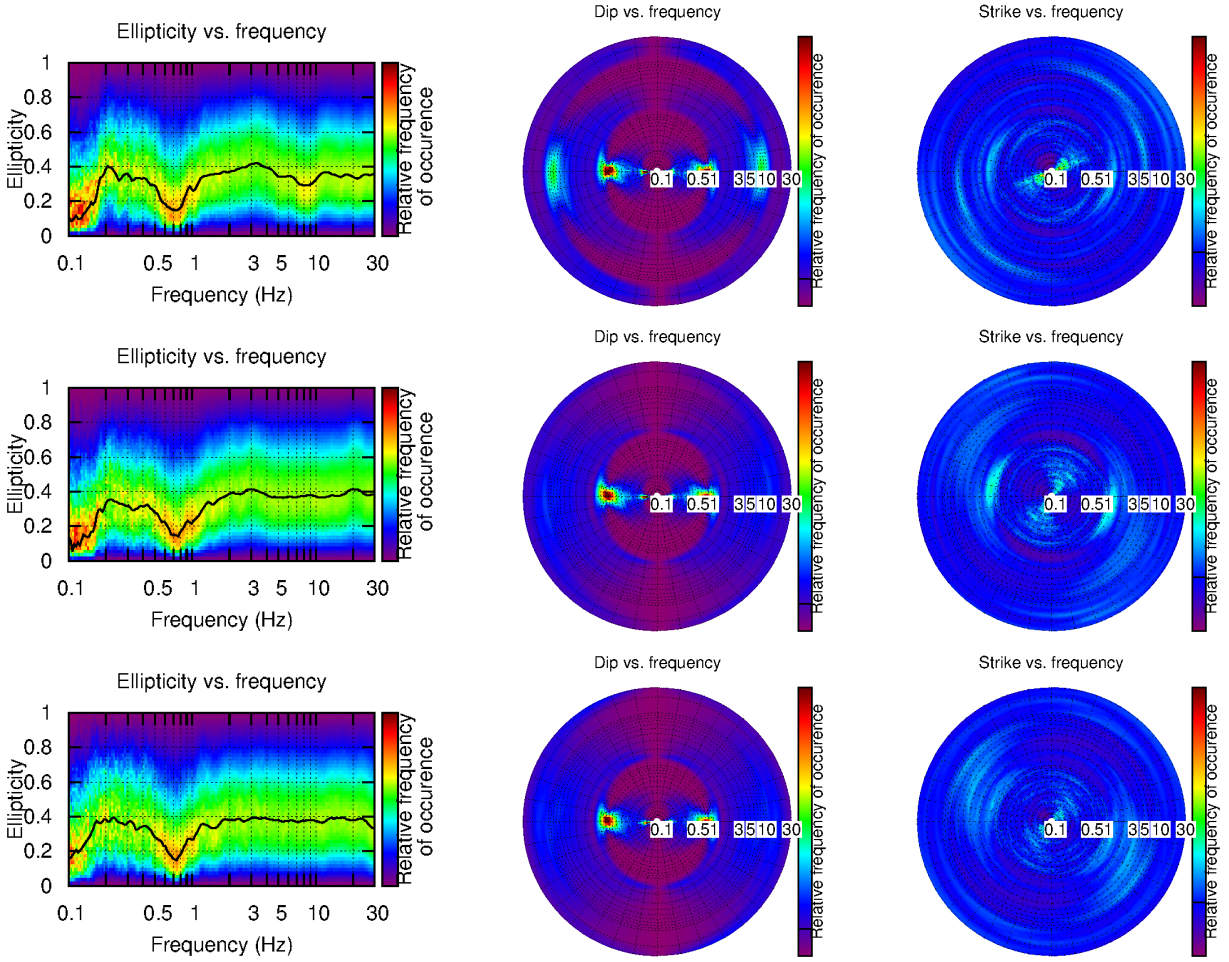

Figure 6: Polarization analysis of stations STHK07, STHK09 and STHK78 (from top to bottom).

4.2.4 3-component high-resolution FK

The results of the 3-component high-resolution FK analysis (Poggi and Fäh, 2010) of both arrays are shown in Figs 7 and 8. On the vertical component, dispersion curves can be clearly identified for both arrays within the array resolution limits, in array 1 between 1.4 and 6.1 Hz and in array 2 between 5.3 and 21.7 Hz. The results on the radial component are less clear, but seem compatible with the vertical component. In array 1, the curve can only be picked between 2.3 and 4.9 Hz, in array 2 between 6.1 and 22.9 Hz. The corresponding ellipticity curves are shown in Fig. 8.
On the transverse component, dispersion curves can also be clearly identified in both arrays. In array 1, the curve can be picked between 1.1 and 7.0 Hz, in array 2 between 5.2 and 34.1 Hz.
Only one mode is visible on all components.

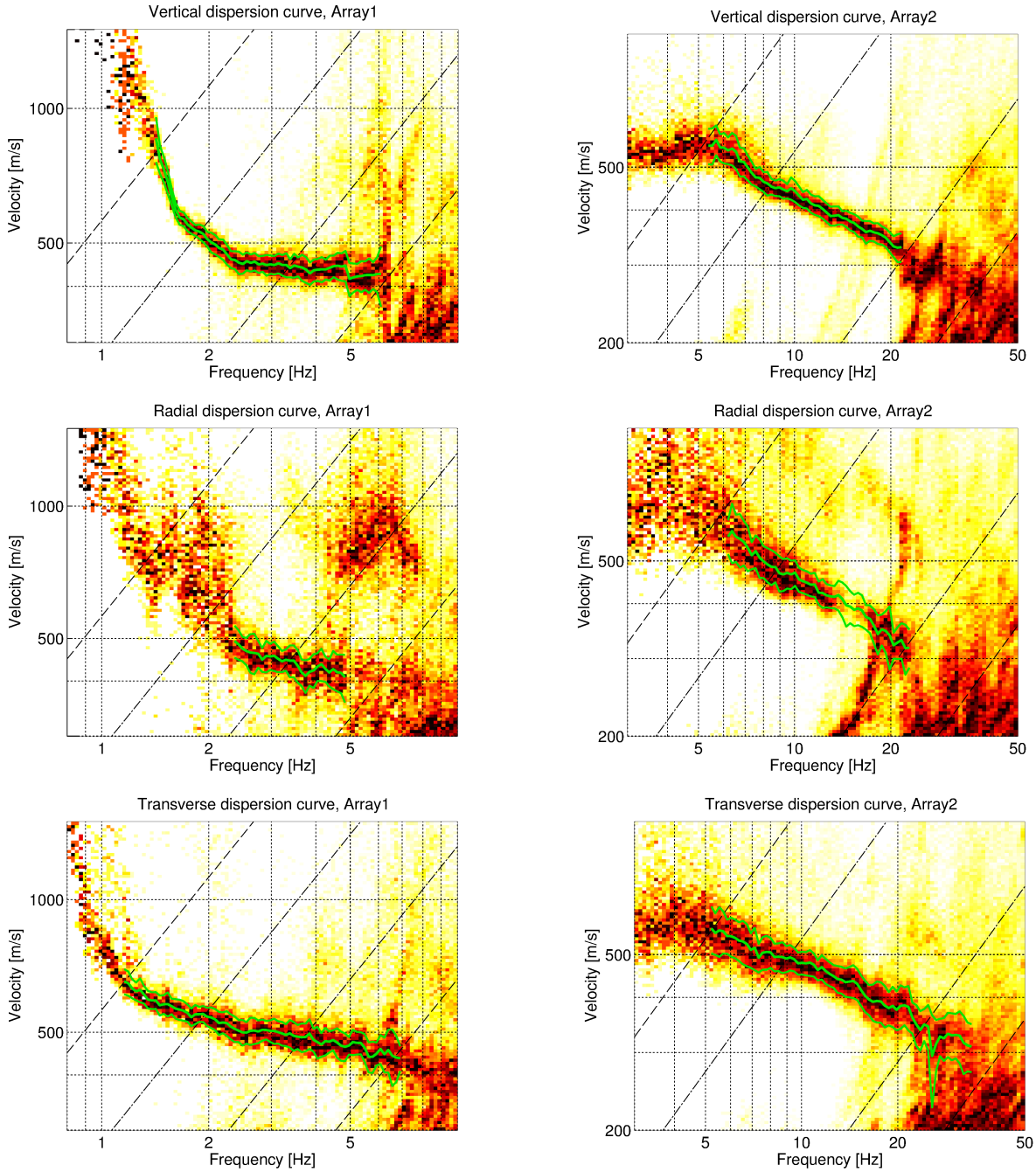

Figure 7: Dispersion curves obtained with the 3-component HRFK algorithm (Poggi and Fäh, 2010). In the left column, the results for array 1 are shown, in the right column for array 2. From top to bottom the results for the vertical, radial and transverse components are shown. The dashed and dotted black lines are the array resolution limits. The solid green lines are picked from the data, where the central line indicates the best values and the two outer lines the standard deviation.

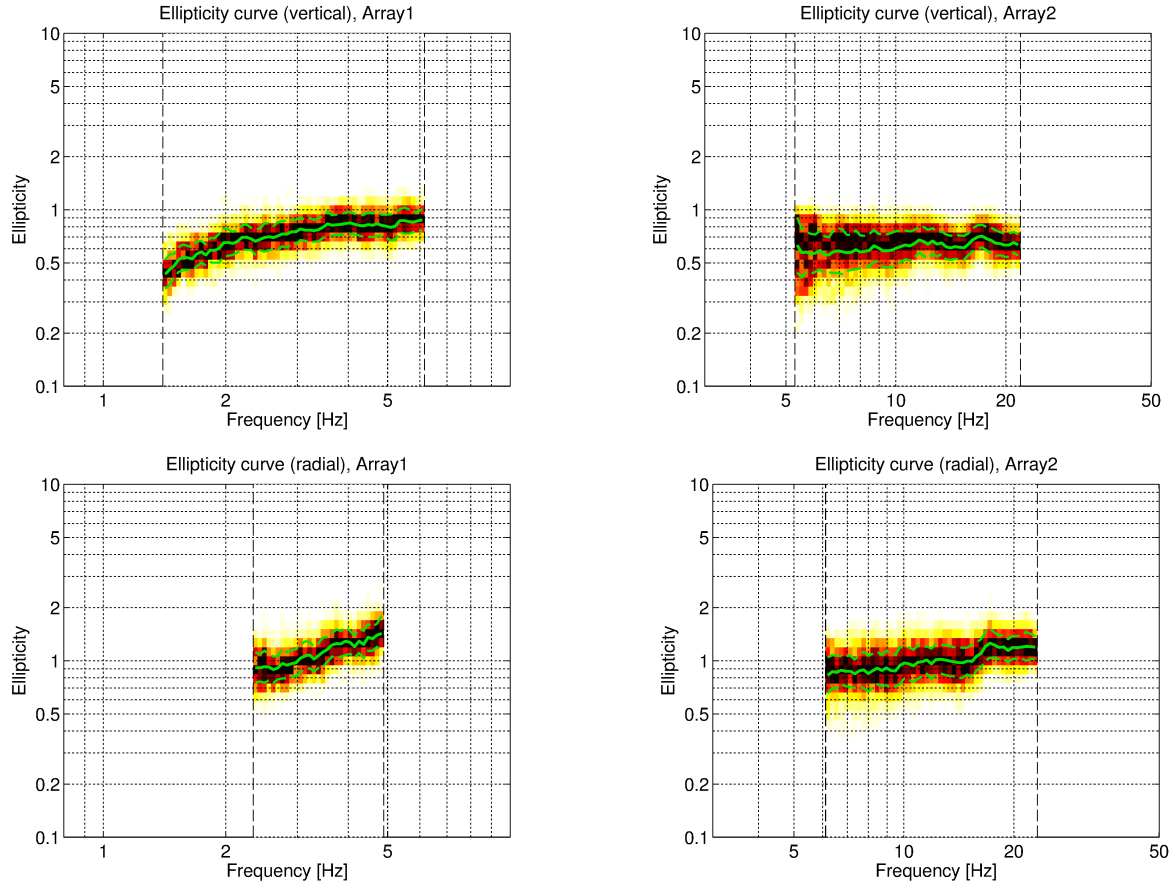

Figure 8: Ellipticity curves obtained with the 3-component HRFK algorithm (Poggi and Fäh, 2010) for the vertical component picked in array 1 (top, left) and array 2 (top, right) and for the radial component for the first mode (bottom, left) and the second mode (bottom, right) picked in array 1. The frequency ranges of the different curves correspond to the ranges where the dispersion curves had been picked.

4.2.5 WaveDec

The results of the WaveDec (Maranò et al., 2012) processing are shown in Fig. 9. This technique estimates the properties of single or multiple waves simultaneously with a maximum likelihood approach. The optimal value of the parameter γ, which modifies the sharpness of the wave property estimation was determined to be 0.3.
The Love wave dispersion curves are clearly retrieved in both arrays, between 1.1 and 5.8 Hz in array 1 and between 5.5 and 22.0 Hz in array 2. The Rayleigh wave dispersion curve is picked between 1.3 and 4.3 Hz in array 1 and between 5.1 and 23.5 Hz. The ellipticity angles for the picked dispersion curves in both arrays are always negative, indicating retrograde particle motion. However, the ellipticity angle in array 1 is becoming positive at the lowermost limit of the picked curve, in agreement with the ellipticity trough identified around 1.5 Hz in Fig. 5.

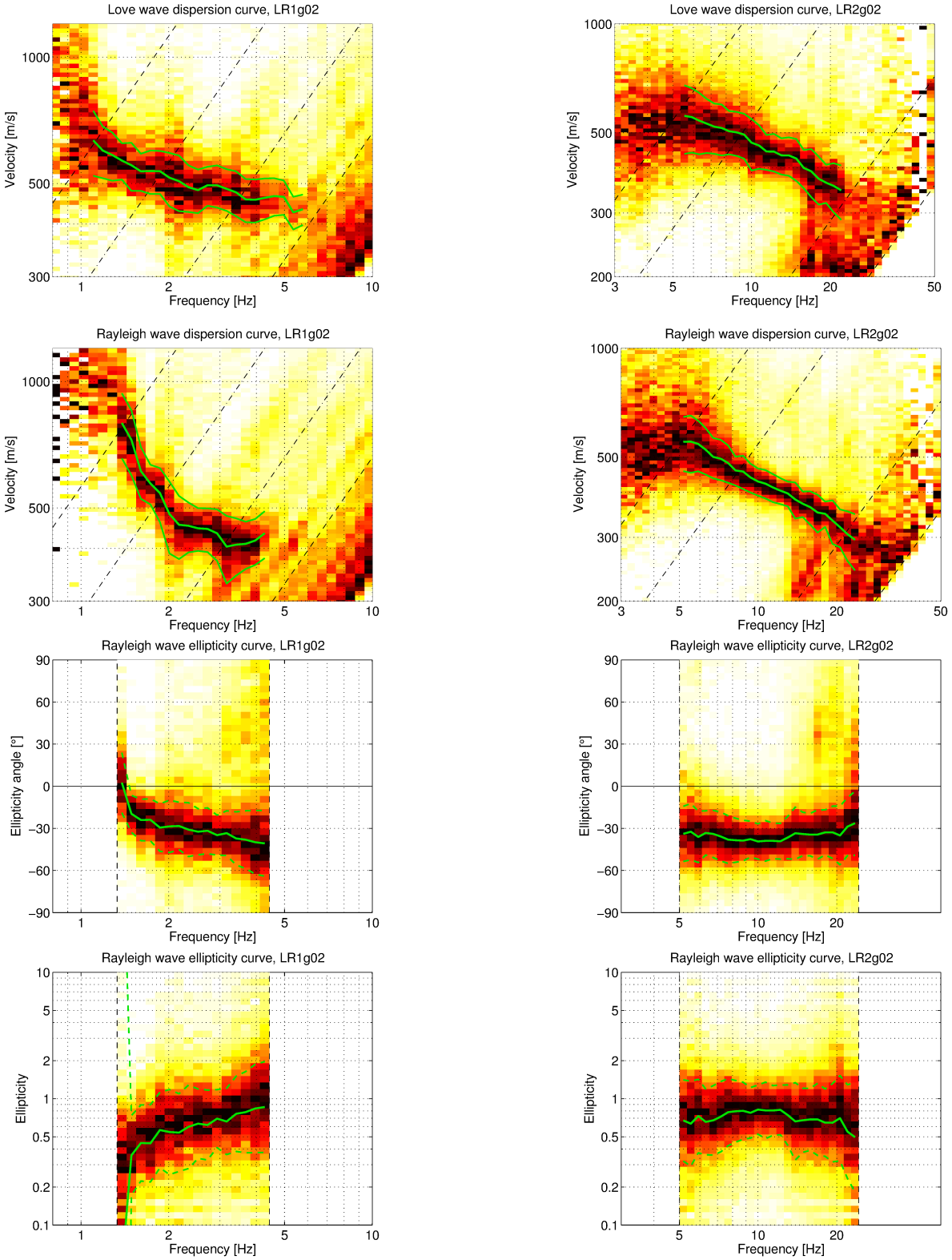

Figure 9: Love and Rayleigh wave dispersion and ellipticity curves obtained with the WaveDec technique (Maranò et al., 2012). The dashed black lines indicate the theoretical array resolution limits. From top to bottom: Love wave dispersion curve, Rayleigh wave dispersion curve, Rayleigh wave ellipticity curve represented as ellipticity angle, Rayleigh wave ellipticity, i.e. the absolute value of the tangent of the ellipticity angle, all for array 1 (left) and array 2 (right).

4.2.6 SPAC

The SPAC (Aki, 1957) curves of the vertical components have been calculated using the M-SPAC (Bettig et al., 2001) technique implemented in geopsy. Rings with different radius ranges had been defined previously and for all station pairs with distance inside this radius range, the cross-correlation was calculated in different frequency ranges. These cross-correlation curves are averaged for all station pairs of the respective ring and give the SPAC curve. The rings are defined in such a way that at least three station pairs contribute and that their connecting vectors have a good directional coverage.
The SPAC curves for all defined rings are shown in Figs 10 and 11, respectively. The black points indicate the data values which contributed to the final dispersion curve estimation, which was made with the function `spac2disp` of the geopsy package. These resulting dispersion curves are shown in Fig. 12.
With array 1, the measured curves are very close to the theoretically expected Bessel functions. From these data, the dispersion curve could be picked between 1.1 and 4.9 Hz. For array 2, the dispersion curve can be obtained in a very wide frequency range between 1.3 and 19.9 Hz.

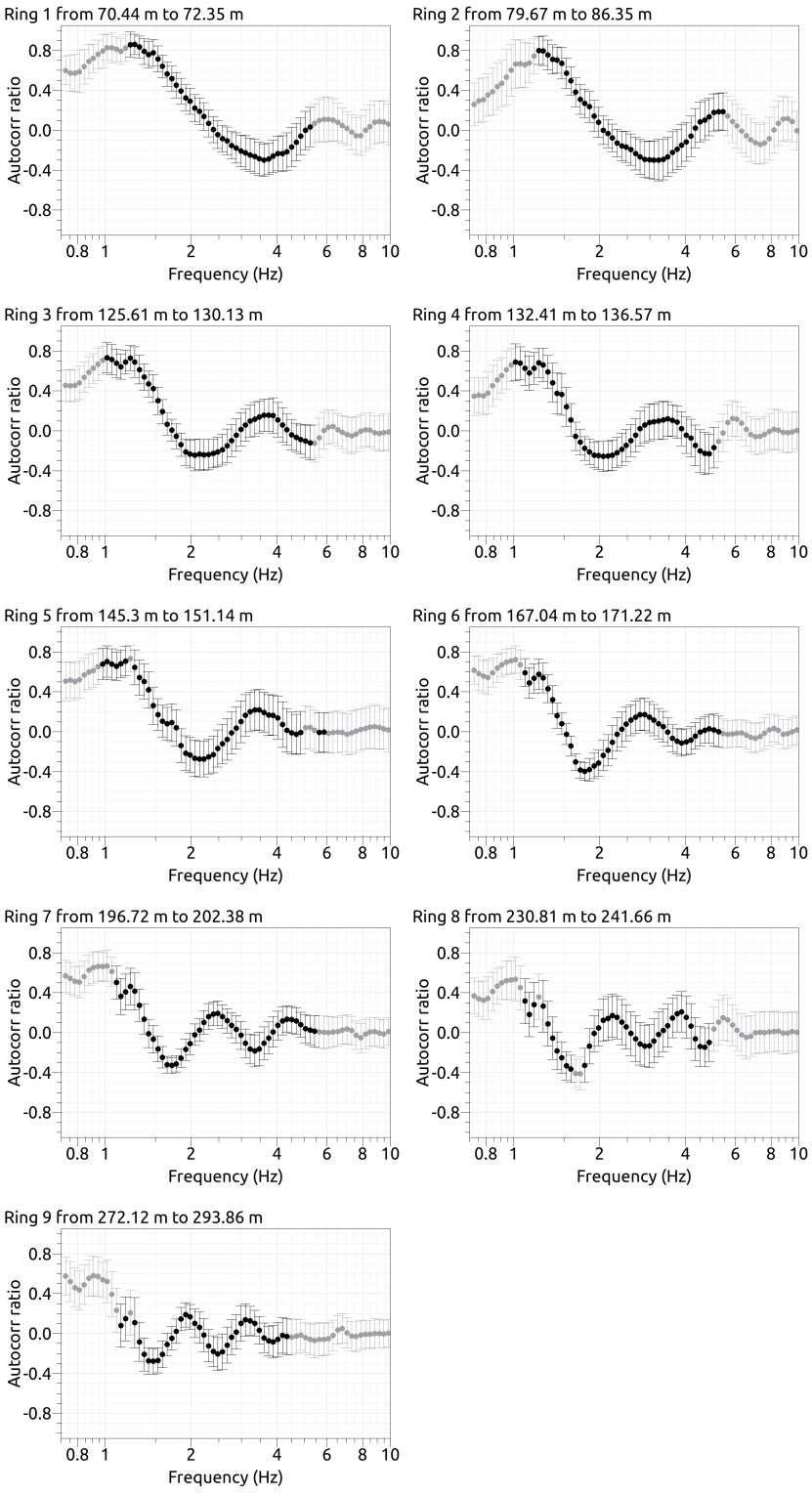

Figure 10: SPAC curves for array 1. The black data points contributed to the dispersion curve estimation.

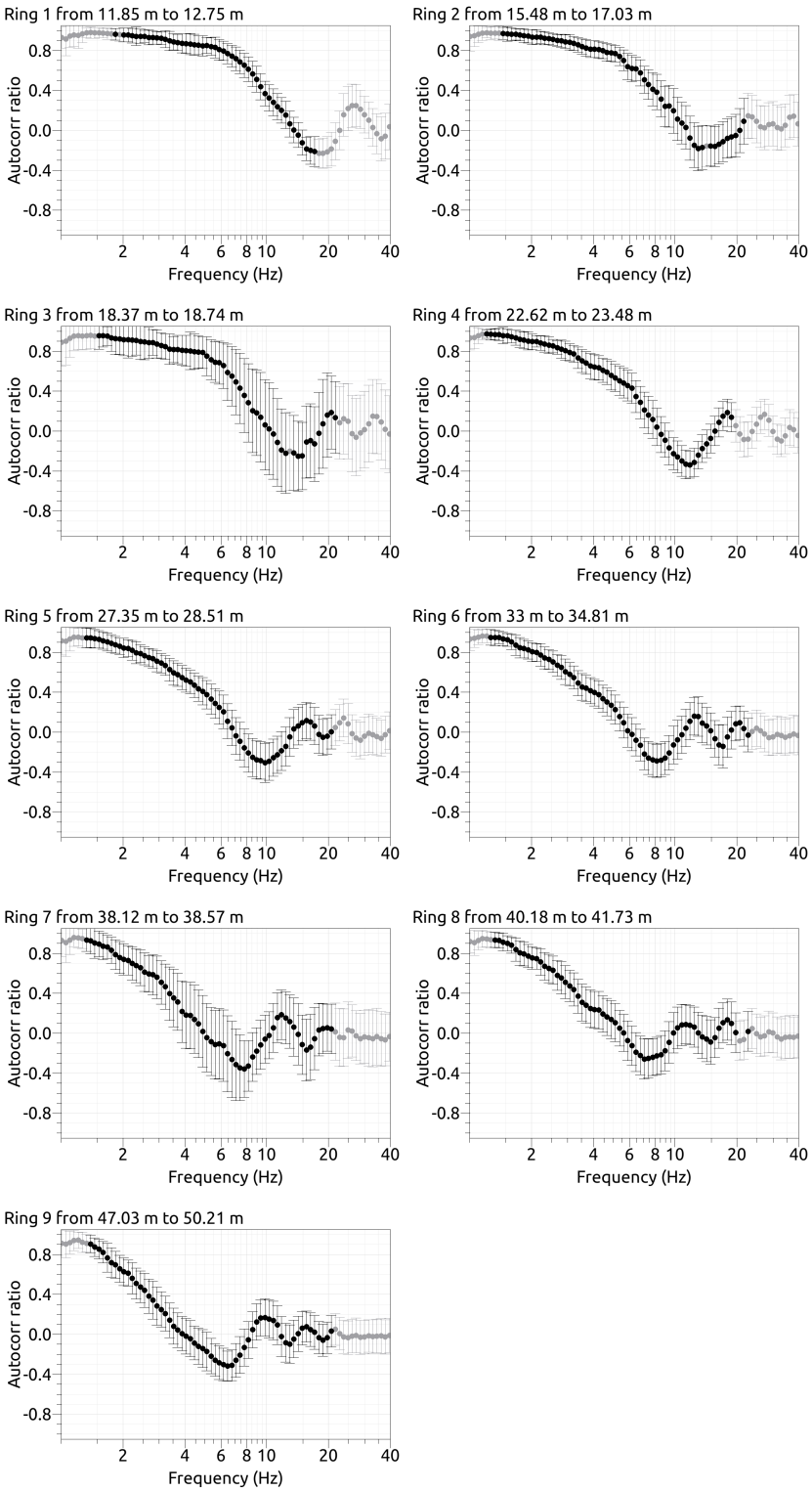

Figure 11: SPAC curves for array 2. The black data points contributed to the dispersion curve estimation.

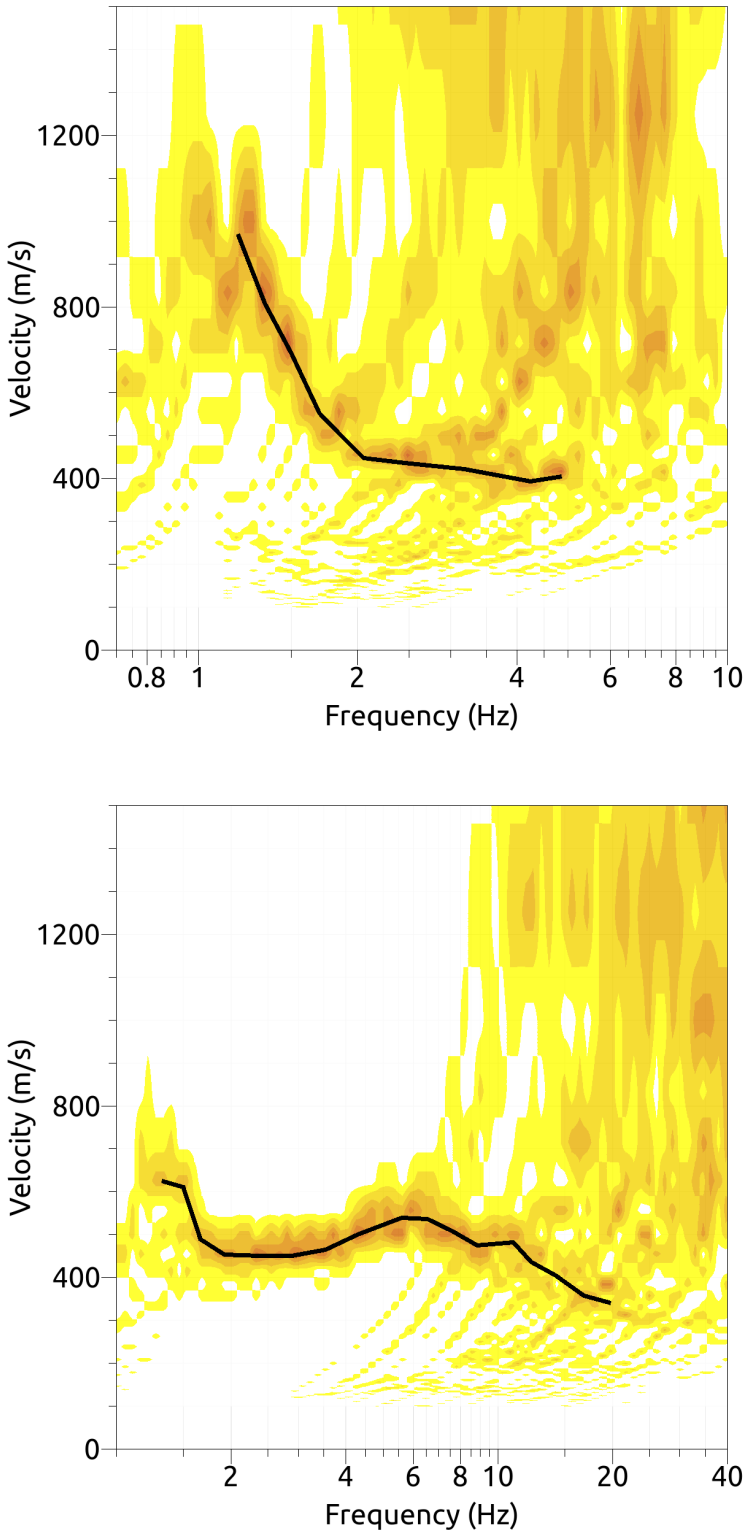

Figure 12: Resulting Rayleigh wave velocities for array 1 (top) and array2 (bottom). The black line corresponds to the picked dispersion curve.

4.3 Summary

Fig. 13 gives an overview of the dispersion and ellipticity curves determined by the different methods.
For Love waves, the HRFK and WaveDec results for the respective arrays are in good agreement, but the curves of both arrays do not seem to match.
For the Rayleigh waves, there is also a very good agreement between the different methods, but a discrepancy between both arrays. The wide dispersion curve measured with SPAC in array 2 proves that the lower-frequency dispersion curves of array 1 are also visible in the area of array 2. This curve suggests that the dispersion curves determined by HRFK or WaveDec in array 2 actually belong to the first higher mode, which is more energetic here than the fundamental mode. We also assume that for the Love waves the dispersion curve of array 2 corresponds to a higher mode.
The ellipticity curves of the different methods are in very good agreement. The arrays were still too small to measure the frequency range of the fundamental ellipticity peak around 0.75 Hz, but the trough around 1.5 Hz is well retrieved by WaveDec. The ellipticity curves from array 2 belong to the first harmonic mode and are a bit lower than the ellipticity of the fundamental peak.

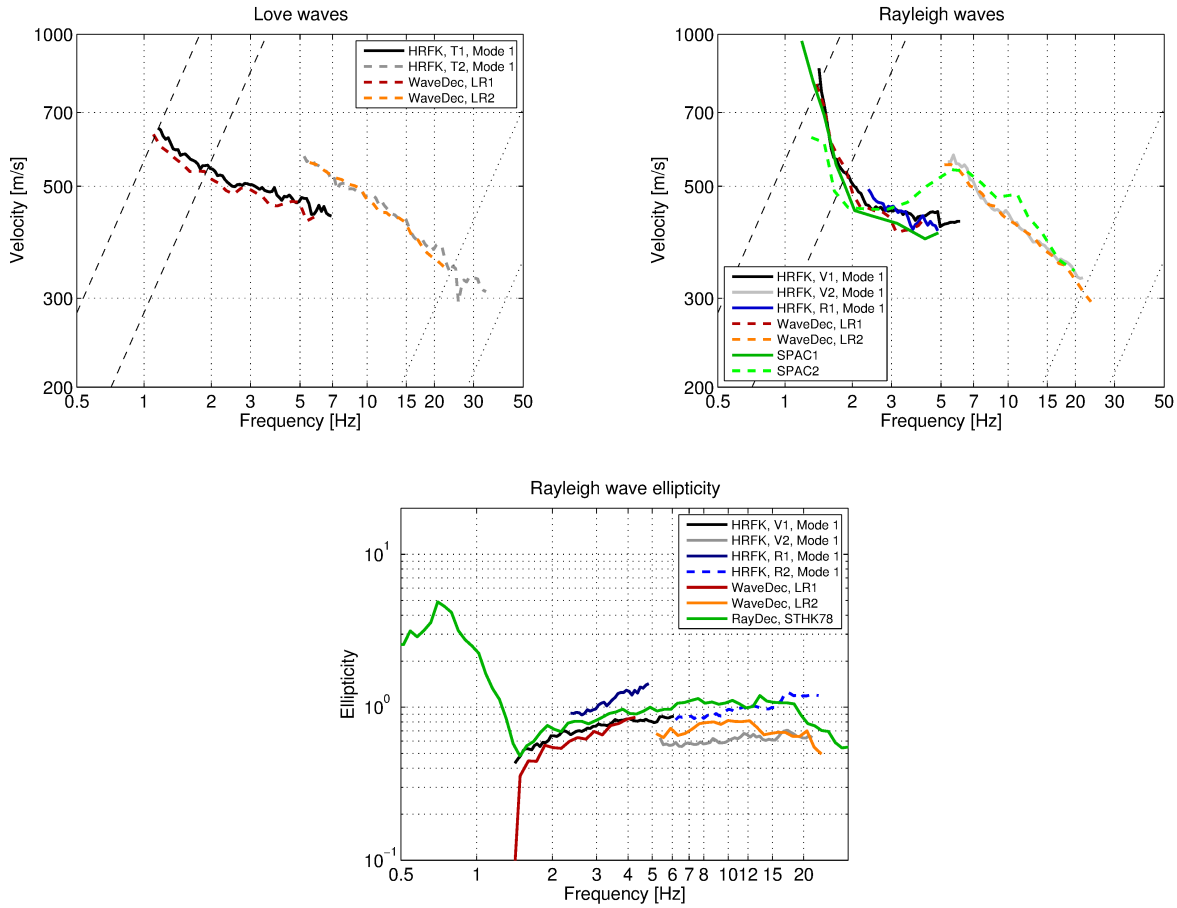

Figure 13: Overview of the Love and Rayleigh wave dispersion curves as well as the ellipticity curves for both arrays. The dashed lines indicate the theoretical resolution limits of the respective arrays (the lower frequency limit corresponds to array 1, the upper one to array 2). The RayDec ellipticity curve corresponds to station STHK78, the station closest to station STHK.

5 Data inversion

5.1 Inversion targets

We performed inversions with two different targets. In the first target, the Rayleigh and Love wave dispersion curves measured with HRFK in array 1 were assumed to correspond to the fundamental mode and the HRFK dispersion curves of array 2 to the first harmonic mode. Additionally, the RayDec curve of STHK78 was used as ellipticity target, but only the left and right flanks of the 0.75 Hz peak and a part beyond the ellipticity trough at 1.5 Hz. The WaveDec ellipticity curve of array 2 was used as ellipticity curve of the first harmonic mode.
For the second inversion target, it was assumed that all measured curves belong to the fundamental mode. Therefore, the dispersion curves of array 1 were cut at low frequency so that the curves of both arrays could fit together. As an ellipticity target, only the RayDec curve of STHK78 was used, the same parts as for the first inversion target.
The details of both inversion targets are indicated in Table 2 and the corresponding curves are shown in Fig. 14.

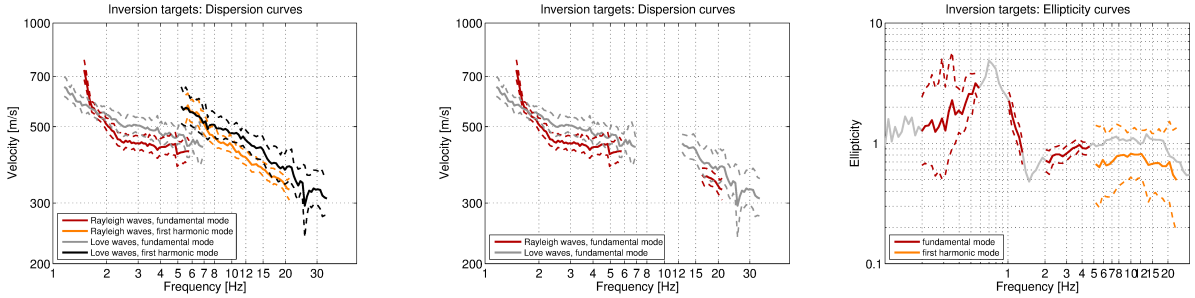

Figure 14: Overview of the dispersion and ellipticity curves used as targets for the different inversions. Left: Dispersion curves for target 1. Center: Dispersion curves for target 2. Right: Ellipticity curves for target 1 (red and orange) and target 2 (red).

Table 2: List of the data curves used as target 1 in the inversion.

Array	Method	Wave type	Mode	Curve type	Frequency range [Hz]
1	HRFK (V)	Rayleigh	fundamental	dispersion	1.4 - 5.8
1	HRFK (T)	Love	fundamental	dispersion	1.1 - 6.8
2	HRFK (V)	Rayleigh	first higher	dispersion	5.7 - 20.8
2	HRFK (T)	Love	first higher	dispersion	5.3 - 33.6
	RayDec (STHK78)	Rayleigh	fundamental	ellipticity	0.2 - 0.6
	RayDec (STHK78)	Rayleigh	fundamental	ellipticity	1.0 - 1.3
	RayDec (STHK78)	Rayleigh	fundamental	ellipticity	2.0 - 4.6
2	WaveDec	Rayleigh	first higher	ellipticity	5.3 - 22.6

Table 3: List of the data curves used as target 2 in the inversion.

Array	Method	Wave type	Mode	Curve type	Frequency range [Hz]
1	HRFK (V)	Rayleigh	fundamental	dispersion	1.4 - 5.8
2	HRFK (V)	Rayleigh	fundamental	dispersion	12.8 - 20.8
1	HRFK (T)	Love	fundamental	dispersion	1.1 - 6.8
2	HRFK (T)	Love	fundamental	dispersion	16.3 - 33.6
	RayDec (STHK78)	Rayleigh	fundamental	ellipticity	0.2 - 0.6
	RayDec (STHK78)	Rayleigh	fundamental	ellipticity	1.0 - 1.3
	RayDec (STHK78)	Rayleigh	fundamental	ellipticity	2.0 - 4.6

5.2 Inversion parameterization

For the inversion, seven different parameterizations have been used. The first six had free values of the depths and velocities of the different layers, ranging from three to eight layers (including the half-space). The last parameterization had fixed layer depths and consisted of 20 layers in total. In each parameterization, the lowest layers were allowed to range down to 300 m depth, for the fixed-depth inversion the lowest interface was located at 250 m depth. The minimum possible shear-wave velocity of the top layer was 50 m/s (v_P to 100 m/s). The density was fixed to 2 300 kg/m^3 for the lowest layer and to 2 000 kg/m^3 for all other layers.
For the inversions with the second target (marked by an attached '1m' to the name of the respective inversion of the first target), only four inversion runs were performed, three with six to eight layers and another one with the fixed-depth approach.

5.3 Inversion results

We performed a total of 11 inversions with different parameterizations (see Table 4). Each inversion run produced 200 000 total models in order to assure a good convergence of the solution. The results of these inversions are shown in Figs 15 - 25.
For the different inversion targets, all inversions yielded very similar minimum misfit values. This indicated that they all fitted the data comparably well, but the best models may still slightly differ. For target 2, less data had to be fitted and the overall misfit values were considerably smaller.
For the inversions STHK3l to STHK8l, the fundamental dispersion curves of Love and Rayleigh waves are well fitted. The dispersion curves of the first harmonic modes show systematic deviations. The ellipticity curve of the fundamental Rayleigh wave mode is well fitted and the peak frequency matches well. Also the part of the first harmonic mode matches well with the data. For inversion STHKfix, the fit of the harmonic mode dispersion curves is better, but the fundamental modes are not well fitted any more. The ellipticity curves match equally well as the other inversions.
The inversions interpreting all curves as the fundamental modes give in principle a better fit of all the data, but this is not surprising as the number of data to fit is smaller and the misfit values between target 1 and target 2 are not directly comparable.

Table 4: List of inversions

Inversion	Number of layers	Number of models	Minimum misfit
STHK3l	3	200 000	0.870
STHK4l	4	200 000	0.828
STHK5l	5	200 000	0.889
STHK6l	6	200 000	0.852
STHK7l	7	200 000	0.865
STHK8l	8	200 000	0.861
STHKfix	20	200 000	0.989
STHK6l1m	6	200 000	0.402
STHK7l1m	7	200 000	0.412
STHK8l1m	8	200 000	0.413
STHKfix1m	20	200 000	0.410

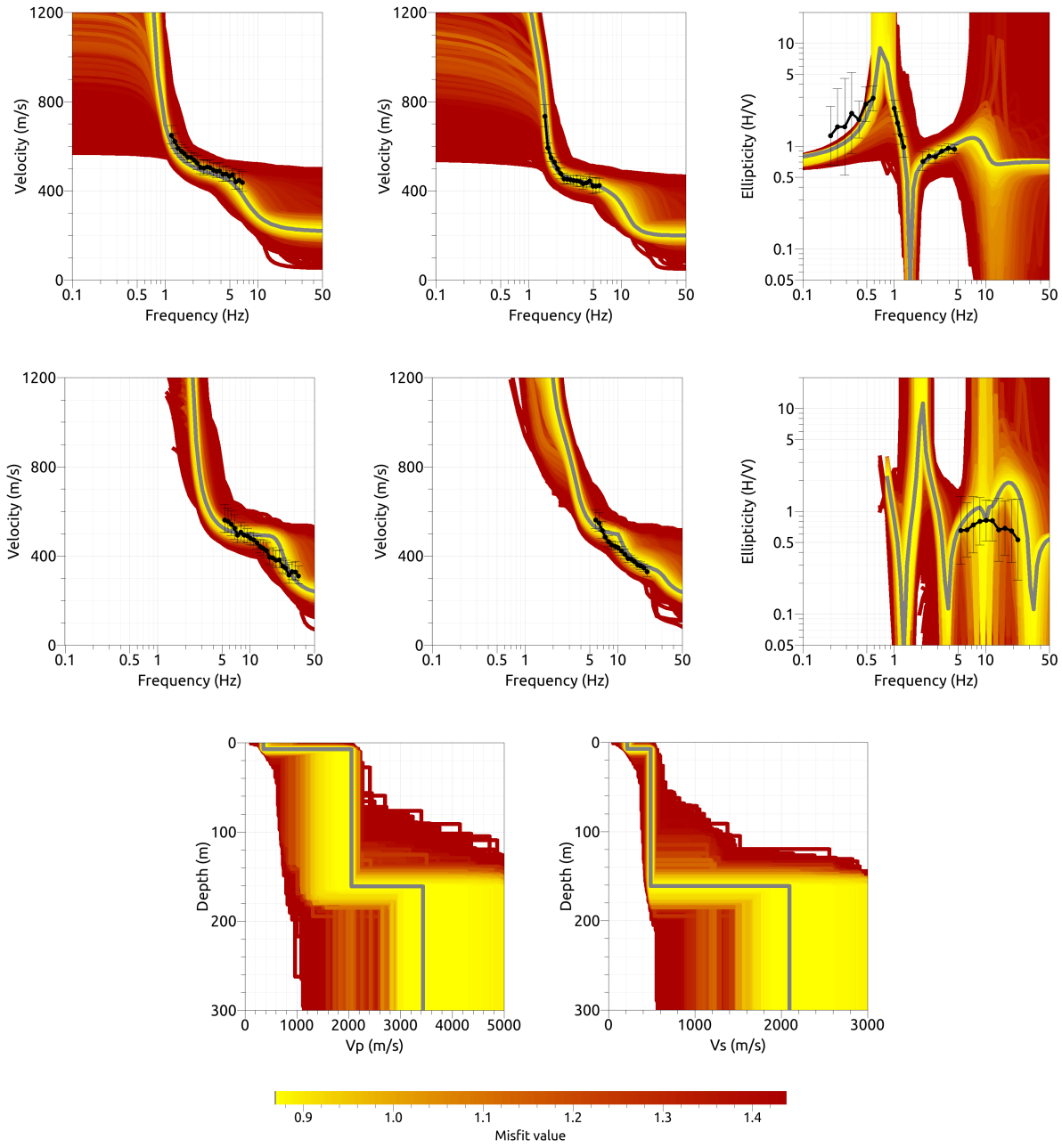

Figure 15: Inversion STHK3l. Top line: Dispersion curves for the Love wave fundamental mode (left) and the Rayleigh wave fundamental mode (center), ellipticity curve for the Rayleigh wave fundamental mode (right). Center line: Dispersion curves for the Love wave first higher mode (left) and the Rayleigh wave first higher mode (center), ellipticity curve for the Rayleigh wave first higher mode (right). Bottom line: P-wave velocity profiles (left) and S-wave velocity profiles (right). The black dots indicate the data points used for the inversion, the gray line indicates the best-fitting model.

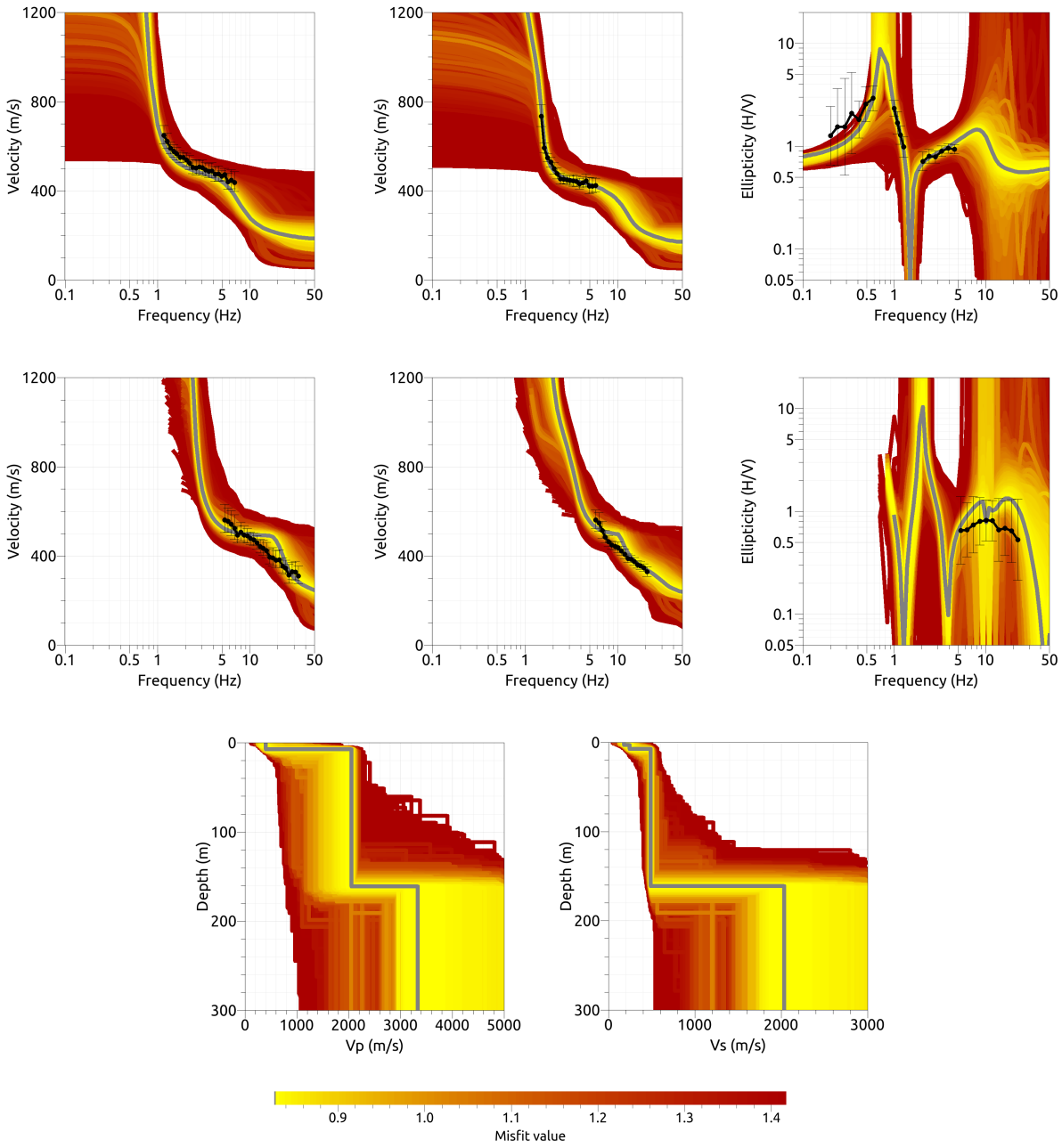

Figure 16: Inversion STHK4l. Top line: Dispersion curves for the Love wave fundamental mode (left) and the Rayleigh wave fundamental mode (center), ellipticity curve for the Rayleigh wave fundamental mode (right). Center line: Dispersion curves for the Love wave first higher mode (left) and the Rayleigh wave first higher mode (center), ellipticity curve for the Rayleigh wave first higher mode (right). Bottom line: P-wave velocity profiles (left) and S-wave velocity profiles (right). The black dots indicate the data points used for the inversion, the gray line indicates the best-fitting model.

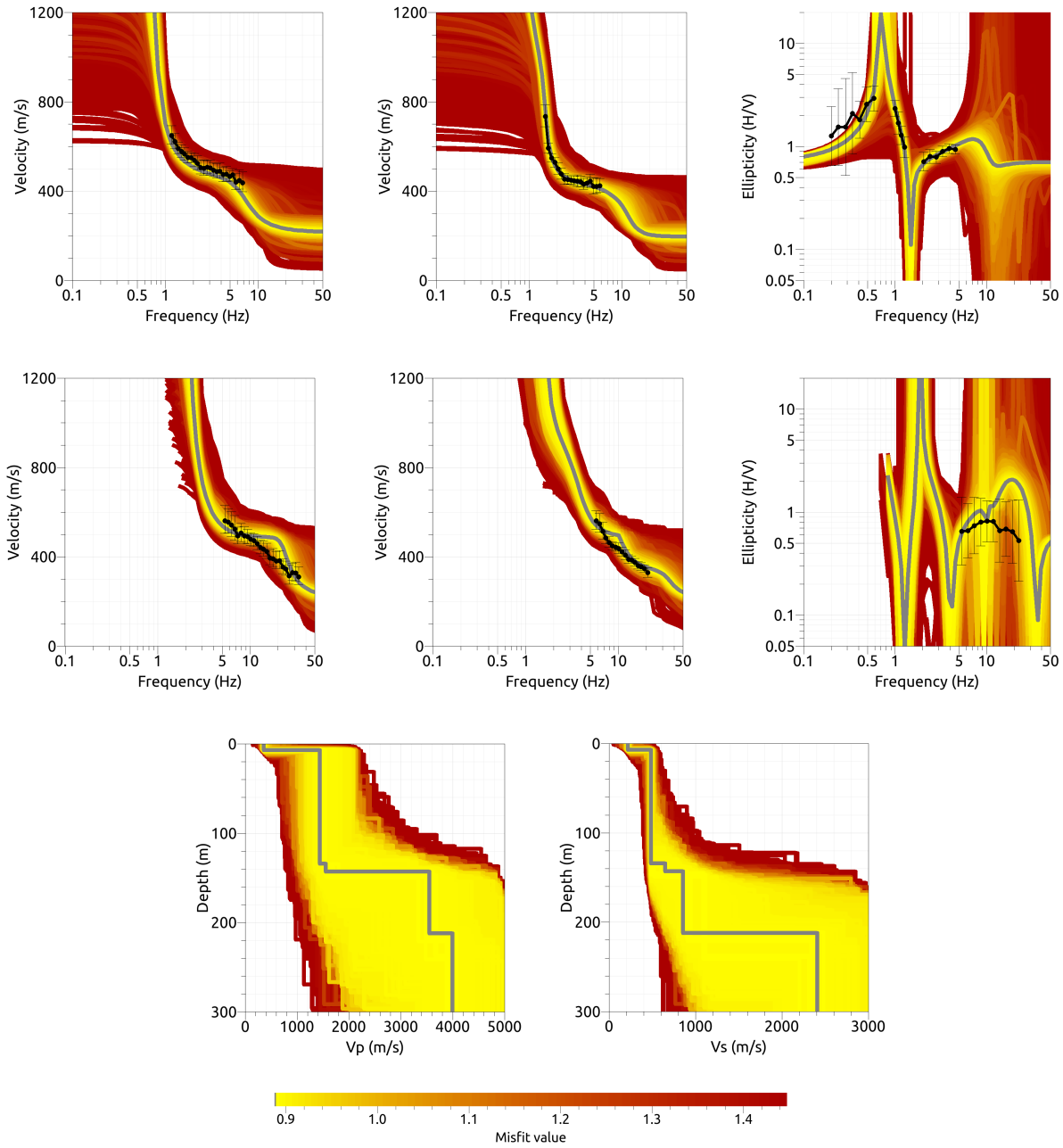

Figure 17: Inversion STHK5l. Top line: Dispersion curves for the Love wave fundamental mode (left) and the Rayleigh wave fundamental mode (center), ellipticity curve for the Rayleigh wave fundamental mode (right). Center line: Dispersion curves for the Love wave first higher mode (left) and the Rayleigh wave first higher mode (center), ellipticity curve for the Rayleigh wave first higher mode (right). Bottom line: P-wave velocity profiles (left) and S-wave velocity profiles (right). The black dots indicate the data points used for the inversion, the gray line indicates the best-fitting model.

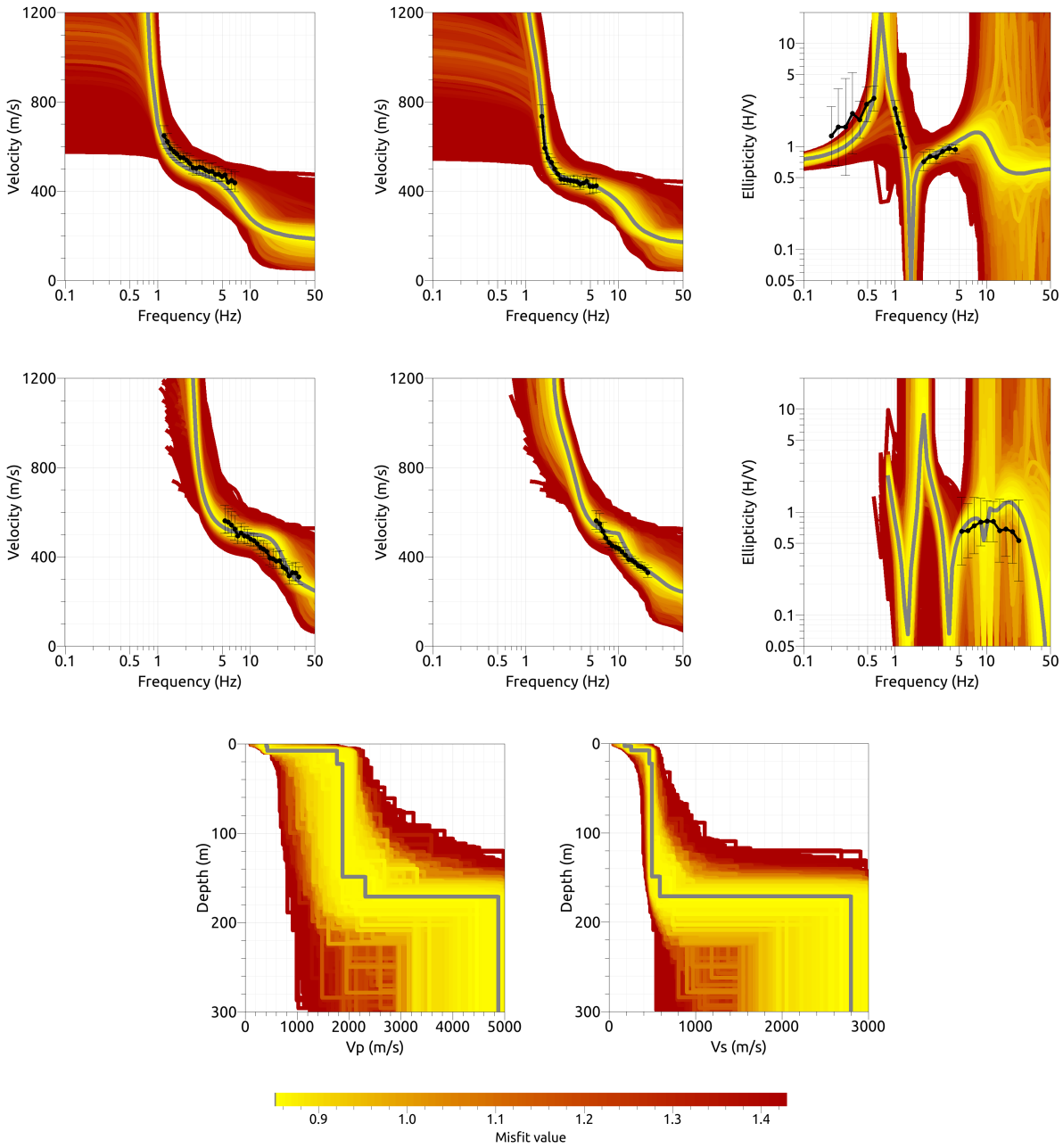

Figure 18: Inversion STHK6l. Top line: Dispersion curves for the Love wave fundamental mode (left) and the Rayleigh wave fundamental mode (center), ellipticity curve for the Rayleigh wave fundamental mode (right). Center line: Dispersion curves for the Love wave first higher mode (left) and the Rayleigh wave first higher mode (center), ellipticity curve for the Rayleigh wave first higher mode (right). Bottom line: P-wave velocity profiles (left) and S-wave velocity profiles (right). The black dots indicate the data points used for the inversion, the gray line indicates the best-fitting model.

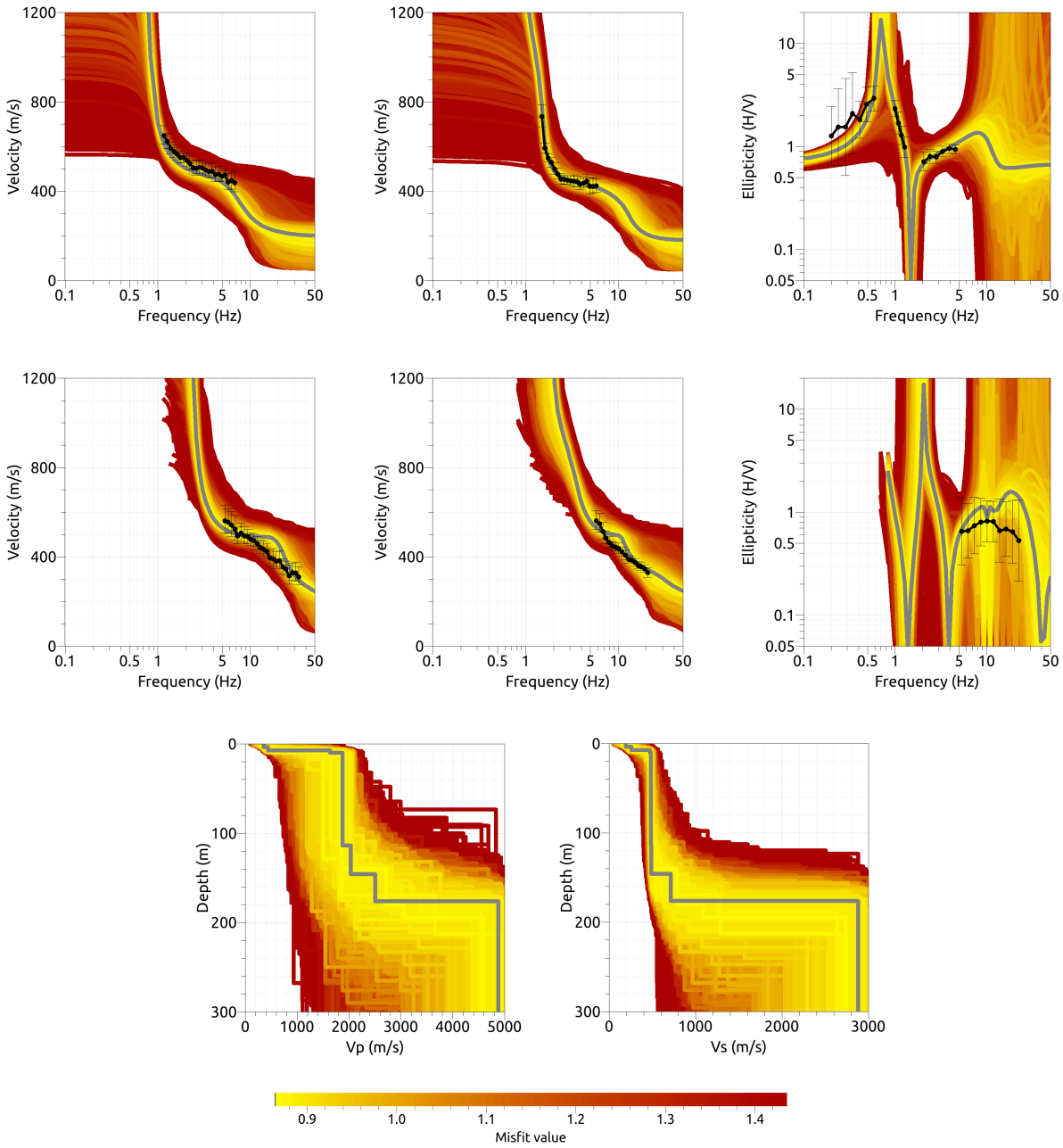

Figure 19: Inversion STHK7l. Top line: Dispersion curves for the Love wave fundamental mode (left) and the Rayleigh wave fundamental mode (center), ellipticity curve for the Rayleigh wave fundamental mode (right). Center line: Dispersion curves for the Love wave first higher mode (left) and the Rayleigh wave first higher mode (center), ellipticity curve for the Rayleigh wave first higher mode (right). Bottom line: P-wave velocity profiles (left) and S-wave velocity profiles (right). The black dots indicate the data points used for the inversion, the gray line indicates the best-fitting model.

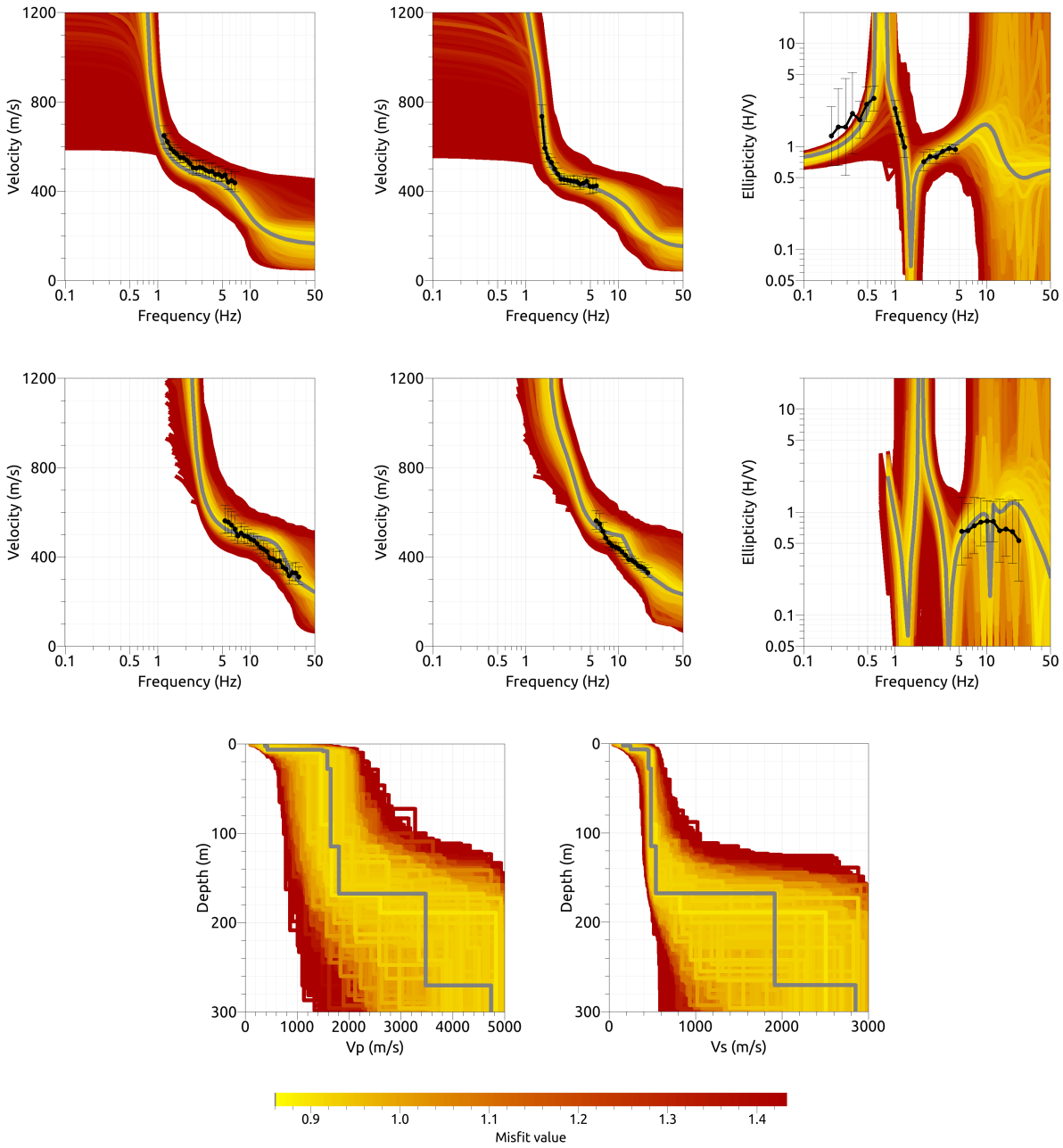

Figure 20: Inversion STHK8l. Top line: Dispersion curves for the Love wave fundamental mode (left) and the Rayleigh wave fundamental mode (center), ellipticity curve for the Rayleigh wave fundamental mode (right). Center line: Dispersion curves for the Love wave first higher mode (left) and the Rayleigh wave first higher mode (center), ellipticity curve for the Rayleigh wave first higher mode (right). Bottom line: P-wave velocity profiles (left) and S-wave velocity profiles (right). The black dots indicate the data points used for the inversion, the gray line indicates the best-fitting model.

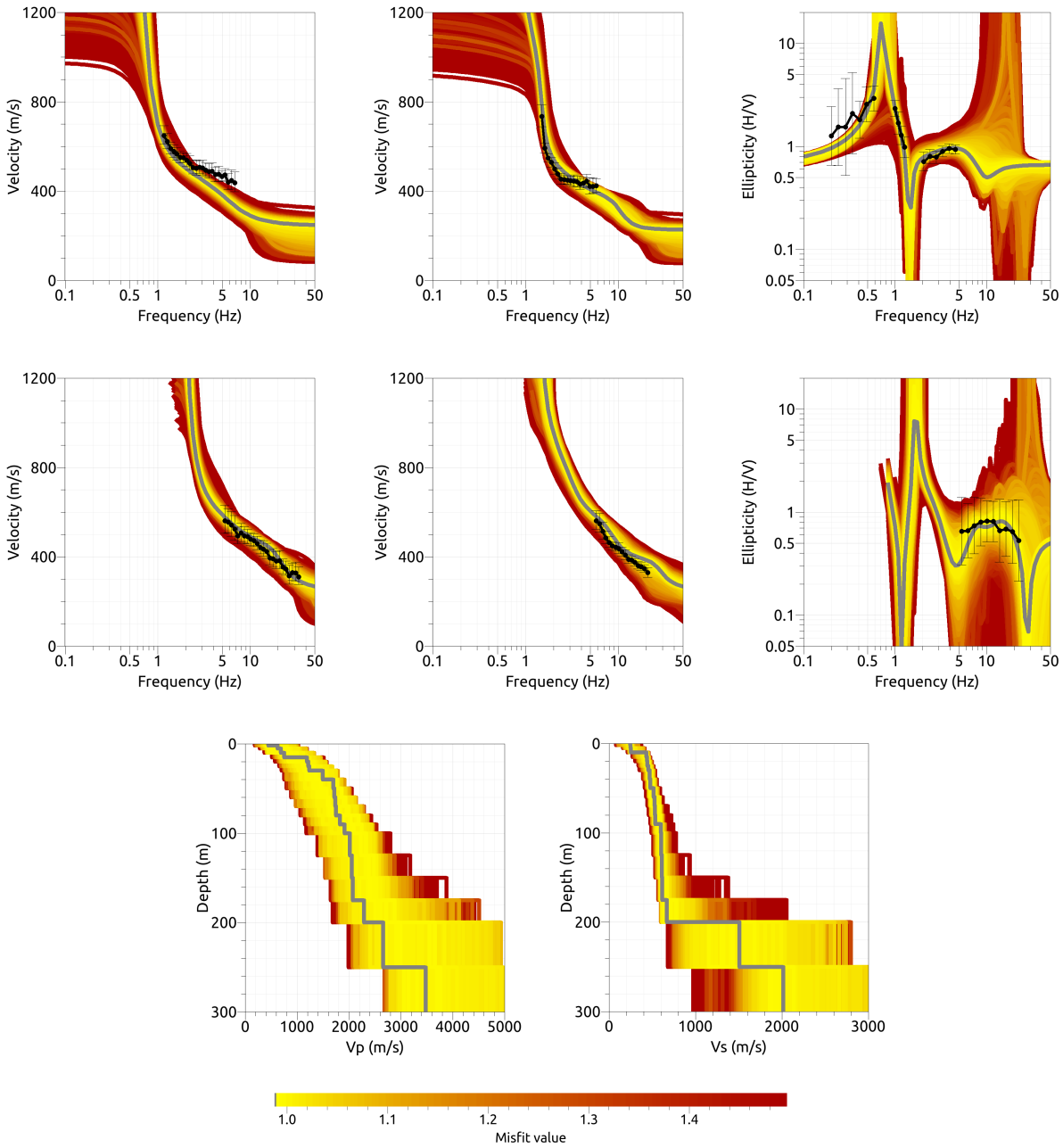

Figure 21: Inversion STHKfix. Top line: Dispersion curves for the Love wave fundamental mode (left) and the Rayleigh wave fundamental mode (center), ellipticity curve for the Rayleigh wave fundamental mode (right). Center line: Dispersion curves for the Love wave first higher mode (left) and the Rayleigh wave first higher mode (center), ellipticity curve for the Rayleigh wave first higher mode (right). Bottom line: P-wave velocity profiles (left) and S-wave velocity profiles (right). The black dots indicate the data points used for the inversion, the gray line indicates the best-fitting model.

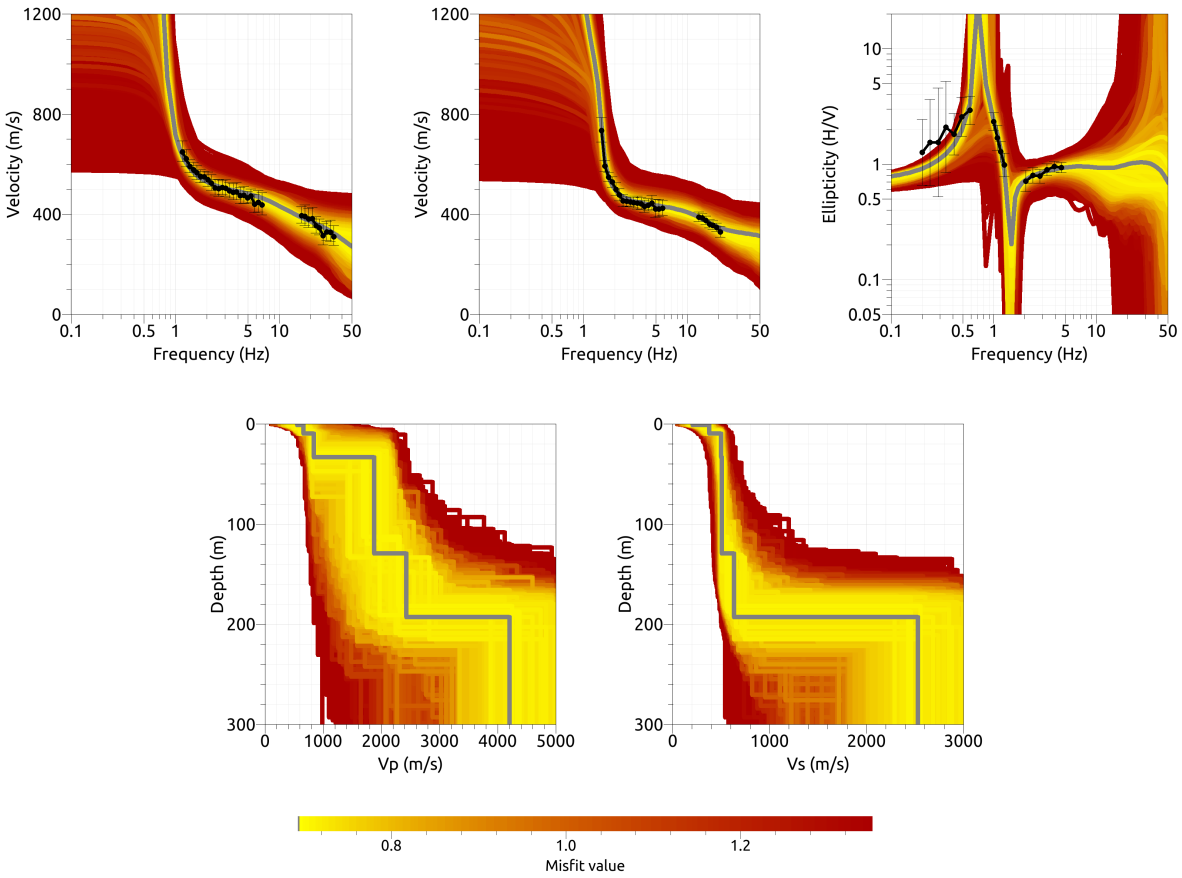

Figure 22: Inversion STHK6l1m. Top line: Love wave fundamental mode (left) and Rayleigh wave fundamental mode (center) dispersion curves, Rayleigh wave ellipticity curve of the fundamental mode (right). Bottom line: P-wave velocity profiles (left) and S-wave velocity profiles (right). The black dots indicate the data points used for the inversion, the gray line indicates the best-fitting model.

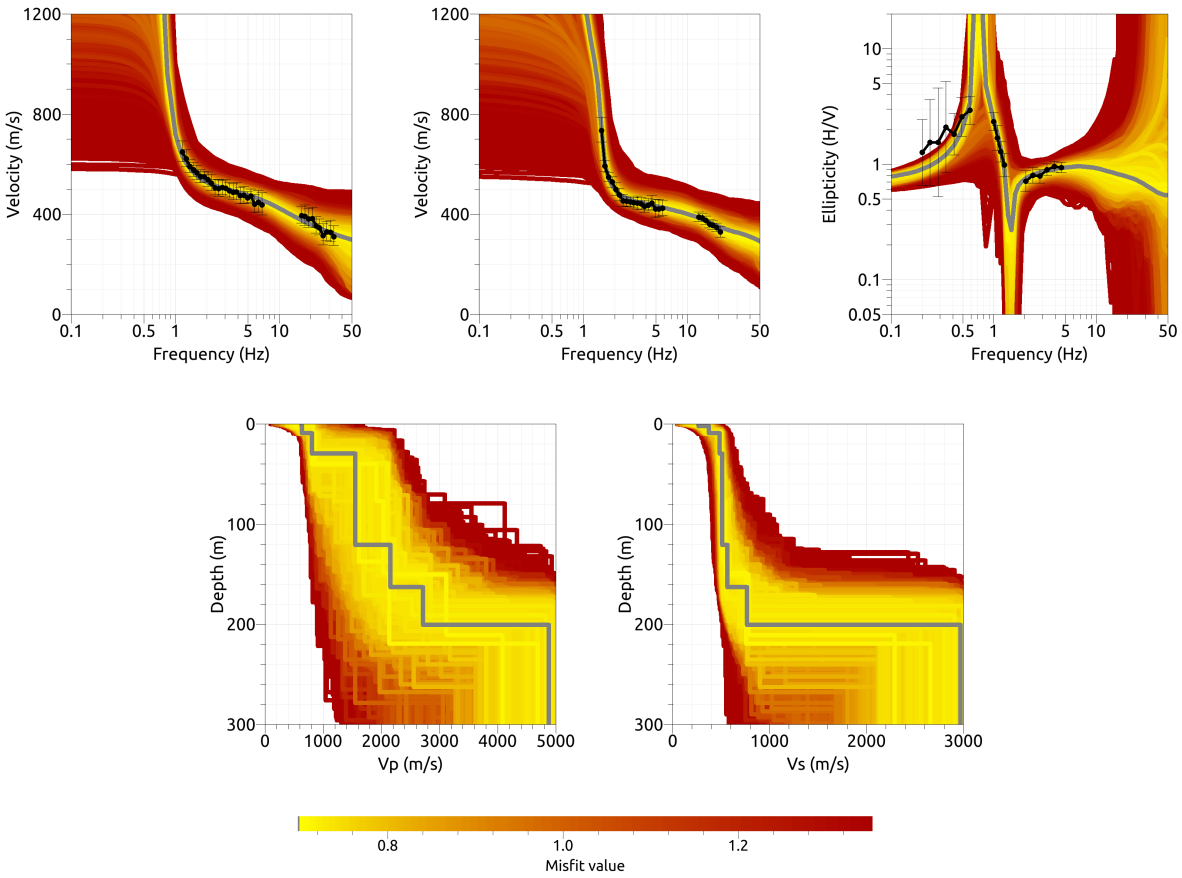

Figure 23: Inversion STHK7l1m. Top line: Love wave fundamental mode (left) and Rayleigh wave fundamental mode (center) dispersion curves, Rayleigh wave ellipticity curve of the fundamental mode (right). Bottom line: P-wave velocity profiles (left) and S-wave velocity profiles (right). The black dots indicate the data points used for the inversion, the gray line indicates the best-fitting model.

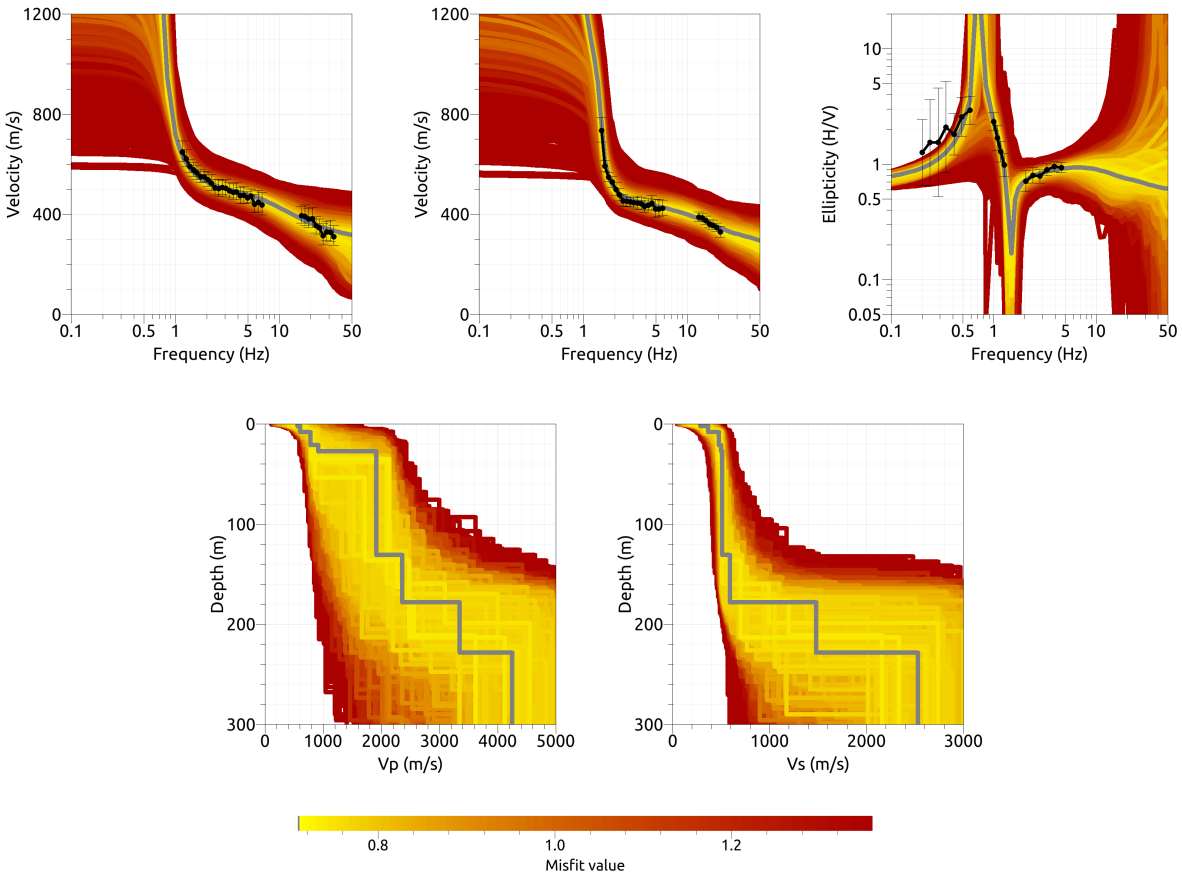

Figure 24: Inversion STHK8l1m. Top line: Love wave fundamental mode (left) and Rayleigh wave fundamental mode (center) dispersion curves, Rayleigh wave ellipticity curve of the fundamental mode (right). Bottom line: P-wave velocity profiles (left) and S-wave velocity profiles (right). The black dots indicate the data points used for the inversion, the gray line indicates the best-fitting model.

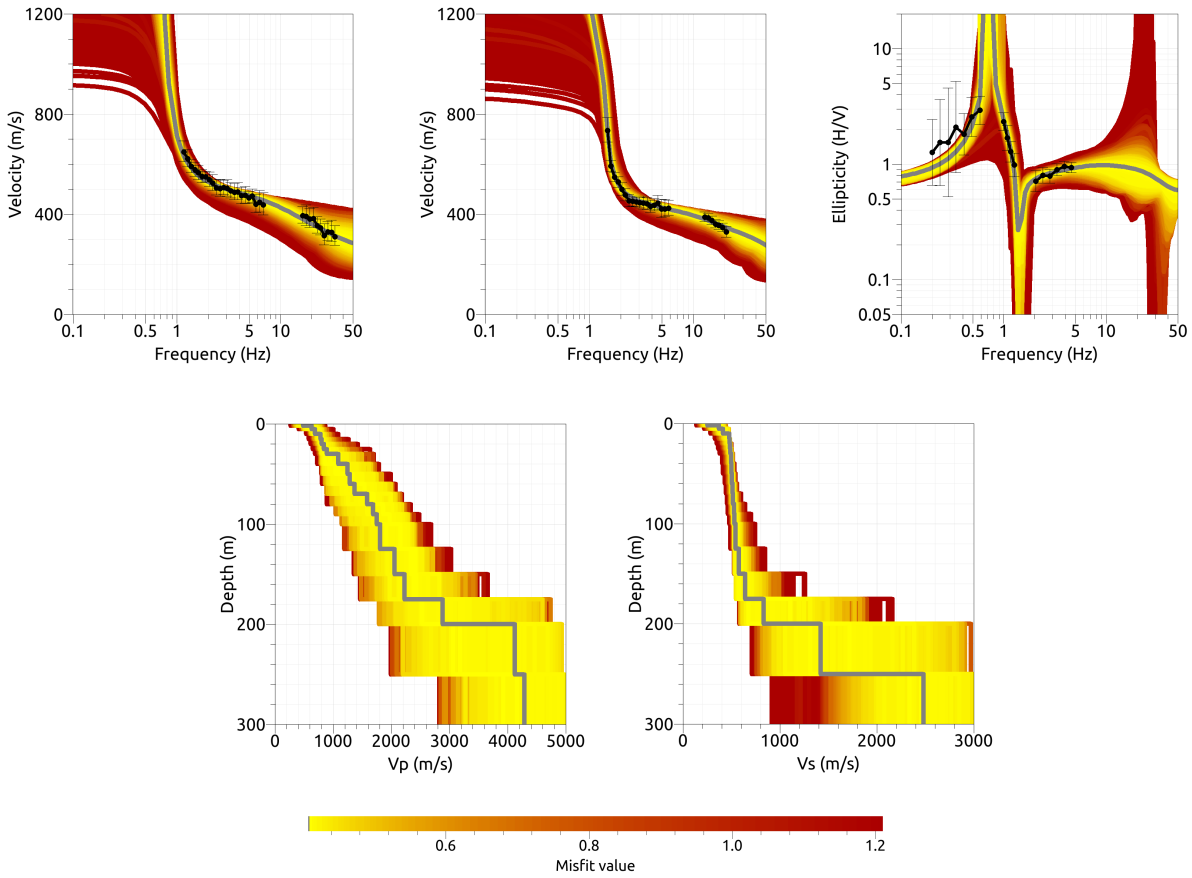

Figure 25: Inversion STHKfix1m. Top line: Love wave fundamental mode (left) and Rayleigh wave fundamental mode (center) dispersion curves, Rayleigh wave ellipticity curve of the fundamental mode (right). Bottom line: P-wave velocity profiles (left) and S-wave velocity profiles (right). The black dots indicate the data points used for the inversion, the gray line indicates the best-fitting model.

5.4 Discussion of the inversion result

The best-fitting models of all inversions are shown in Fig. 26. There are clear differences between the inversions including higher modes and the inversions interpreting all measurements as the fundamental modes, especially in the shallow part above 10 m of depth. The latter inversions have systematically larger velocity values. This results in differences in the V_{S30} values as well, for the inversions with the first target, they range from 351 to 377 m/s (368 $\pm$ 9 m/s). For the inversions with the second target, they range from 431 to 436 m/s (433 $\pm$ 3 m/s). The inversions with target 1 give velocity models with a first strong impedance contrast at about 7 m, with shear-wave velocities around 200 m/s in the superficial layer. The inversions with target 2 yield faster shallow structures, with a first layer of 2 m depth and velocities between 200 and 300 m/s, followed by a second layer down to 8 to 10 m with S-wave velocities of about 370 m/s.
In the depth range between 10 and 150 m, all velocity profiles look more similar and have shear-wave velocities around 500 m/s, but also here the inversions with target 2 have slightly higher velocity values than the ones with target 1. The seismic bedrock is found between 160 and 210 m for all inversions.

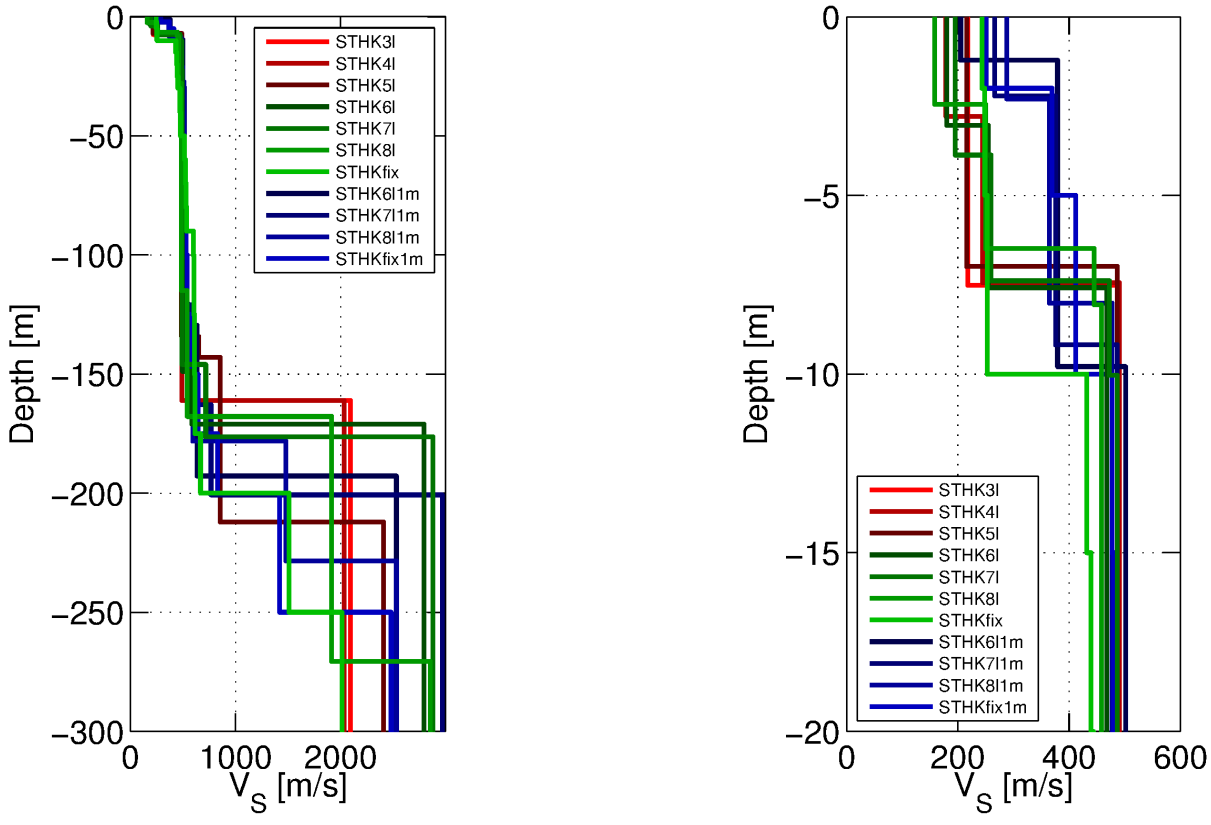

Figure 26: Overview of shear-wave velocity profiles of the best-fitting models of all inversions (left) and a zoom on the shallow part (right).

5.5 SH transfer function

The empirical amplification for station STHK is based on only six events so far (21 April 2017) and the statistical quality of the curve will certainly increase in the future. In Fig. 27, the theoretical shear-wave transfer functions for the inversion with targets 1 and 2 are compared with the empirical amplification. At low frequencies, both inversions have virtually identical transfer functions, which show some agreement with the empirical amplification. The flatness of this empirical amplification is a sign of edge-generated surface waves (Michel et al., 2014). At higher frequencies, above about 7 Hz, the empirical amplification is larger than at lower frequencies. The transfer functions for target 1 are higher than those of target 2 in that range. Therefore, target 1 is producing velocity models which are closer to reality than those of target 2 and we conclude that the measured dispersion curves of the smaller array actually belong to the first harmonic modes.

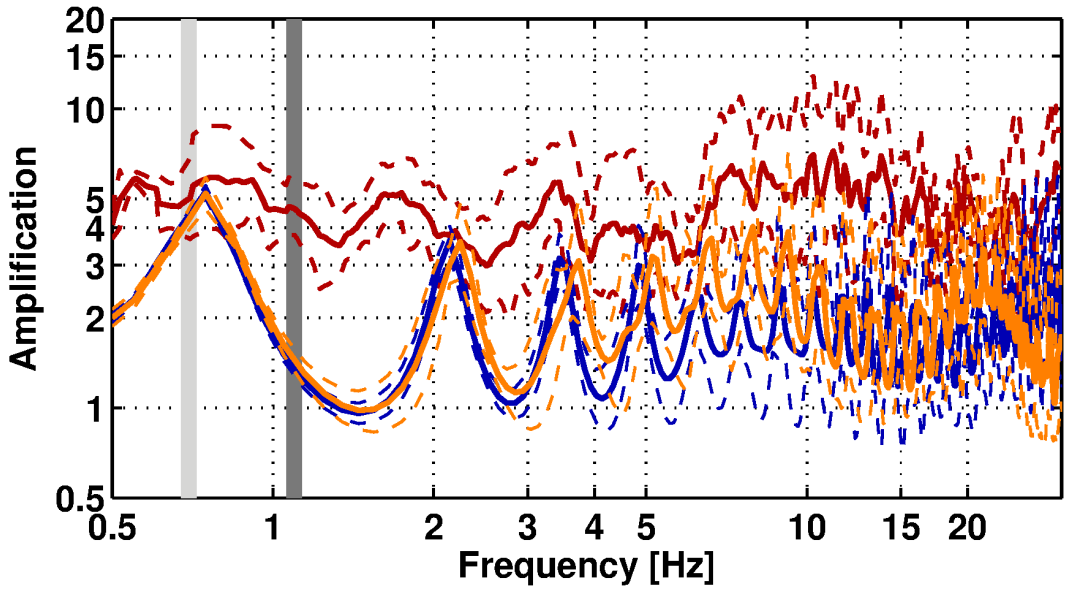

Figure 27: Comparison between the modeled amplification for the best models of the seven different inversions with target 1 (orange, with standard deviation), the inversions with target 2 (blue, with standard deviation) and the empirical amplification measured at station STHK (red, with standard deviation). The vertical light and dark grey bars correspond to the ellipticity peak frequency and the lowest frequency of the dispersion curves, respectively.

5.6 Quarter-wavelength representation

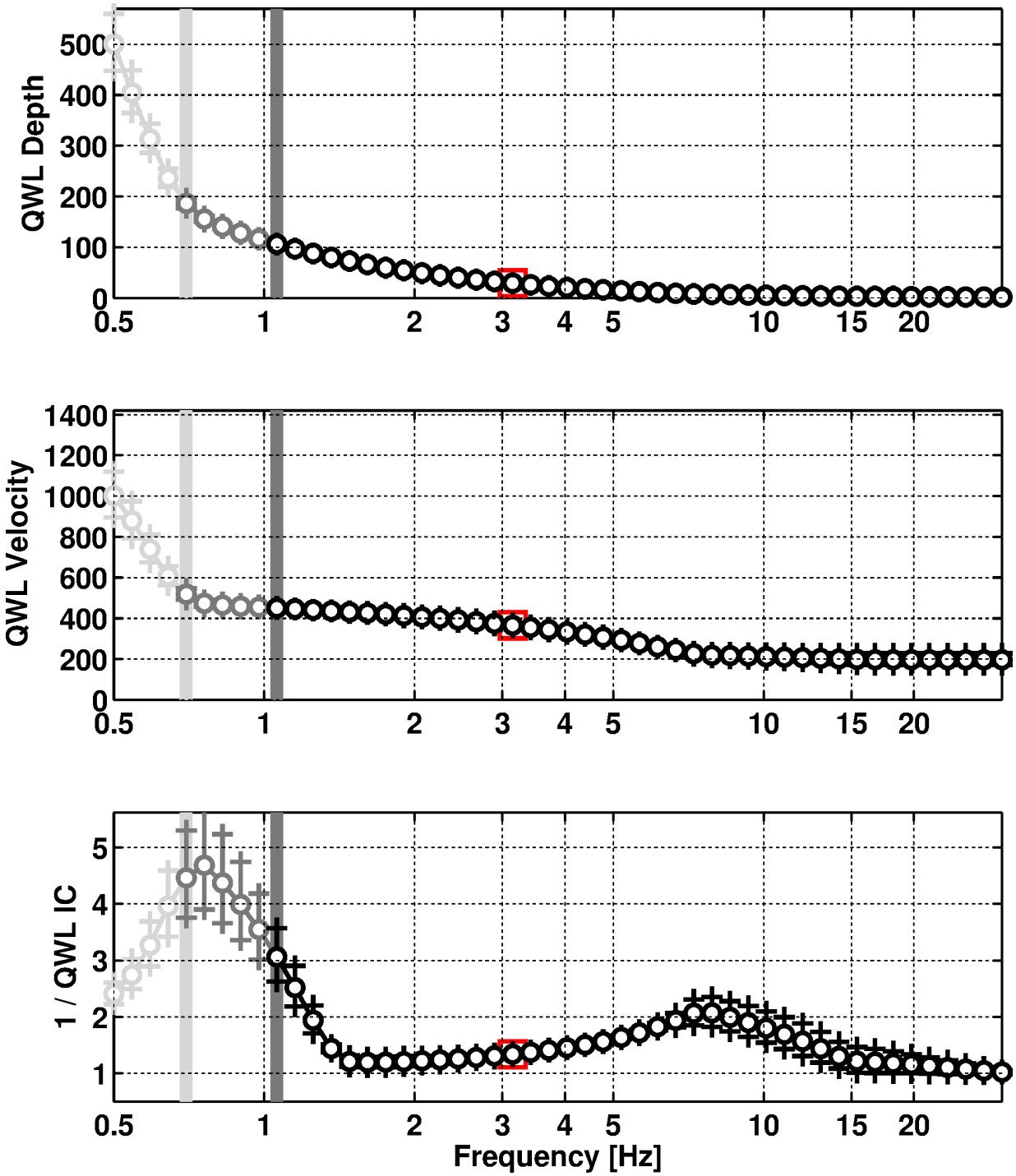

Figure 28: Quarter wavelength representation of the velocity profile for the best models of the inversions with target 1 (top: depth, center: velocity, bottom: inverse of the impedance contrast). The black curves are constrained by the dispersion curves, the light grey curves are not constrained by the data. The red square corresponds to V_{S30}.

6 Conclusion

We performed a passive array measurement with two different configurations to characterize the soil underneath station STHK in Thun (BE), located inside a deep alluvial basin close to the lake shore of Lake Thun.
The dispersion curves for Love and Rayleigh waves could be measured over a wide frequency range. The large and small arrays yield different parts of the dispersion curves. The ellipticity peak frequency is around 0.75 Hz. The final analysis with the comparison between the S-wave transfer functions of the inversion results and the empirical amplification function resulted in the identification of the curves from the larger array as the respective fundamental modes and the curves from the smaller array as the first harmonic modes.
The joint inversion of Love and Rayleigh wave dispersion and ellipticity curves showed that the structure can be explained by models with at least three layers. All inversions show a superficial layer of around 7 m thickness with an S-wave velocity of about 200 m/s, followed by a second main layer of about 500 m/s down to at least 150 m. The interface with the seismic bedrock varies between 150 and 200 m of depth for the different inversion parameterizations. The V_{S30} of the best models is about 370 m/s, corresponding to soil class B in EC8 and C in SIA261.

Acknowledgements

The authors thank Oona Brunner, Marthe Faber and Felicitas Stein for their help during the array measurements.

References

Aki, K. (1957). Space and time spectra of stationary stochastic waves, with special reference to microtremors. *Bull. Earthquake Res. Inst. Tokyo Univ.*, 35:415–456.

Bettig, B., Bard, P.-Y., Scherbaum, F., Riepl, J., Cotton, F., Cornou, C., and Hatzfeld, D. (2001). Analysis of dense array noise measurements using the modified spatial auto-correlation method (SPAC): application to the Grenoble area. *Boll. Geof. Teor. Appl.*, 42:281–304.

Burjánek, J., Gassner-Stamm, G., Poggi, V., Moore, J. R., and Fäh, D. (2010). Ambient vibration analysis of an unstable mountain slope. *Geophys. J. Int.*, 180:820–828.

Burjánek, J., Moore, J. R., Molina, F. X. Y., and Fäh, D. (2012). Instrumental evidence of normal mode rock slope vibration. *Geophys. J. Int.*, 188:559–569.

Fäh, D., Wathelet, M., Kristekova, M., Havenith, H., Endrun, B., Stamm, G., Poggi, V., Burjanek, J., and Cornou, C. (2009). Using ellipticity information for site characterisation. NERIES deliverable JRA4 D4, available at http://www.neries-eu.org.

Hobiger, M., Bard, P.-Y., Cornou, C., and Le Bihan, N. (2009). Single station determination of Rayleigh wave ellipticity by using the random decrement technique (RayDec). *Geophys. Res. Lett.*, 36.

Maranò, S., Reller, C., Loeliger, H.-A., and Fäh, D. (2012). Seismic waves estimation and wavefield decomposition: Application to ambient vibrations. *Geophys. J. Int.*, 191:175–188.

Michel, C., Edwards, B., Poggi, V., Burjánek, J., Roten, D., Cauzzi, C., and Fäh, D. (2014). Assessment of site effects in alpine regions through systematic site characterization of seismic stations. *Bull. Seismol. Soc. Am.*, 104:–.

Poggi, V. and Fäh, D. (2010). Estimating Rayleigh wave particle motion from three-component array analysis of ambient vibrations. *Geophys. J. Int.*, 180:251–267.